

# POLITECNICO DI TORINO

Corso di Laurea Magistrale

in Nuclear and Energy Engineering

Tesi di Laurea Magistrale

Modelling of the flow straightener of a 7 pin ALLEGRO rod  
bundle



Relatori

Cristina Bertani

Attila Aszodi

Gergely Imre Orosz

Candidato

Matthias Peiretti

Formattato: Interlinea: multipla 1.3 ri

ha formattato: Tipo di carattere: 18 pt

Formattato: Interlinea: multipla 1.3 ri

Formattato: Interlinea: multipla 1.3 ri

Formattato: Interlinea: multipla 1.3 ri

Tabella formattata

Formattato: Interlinea: multipla 1.3 ri

|

|

## Abstract

With the progress and the born of new economies with a willingness of fast growth, the global demand of energy has increased constantly. For these reasons, the world is currently experiencing an increasing need for development of sustainable, low-carbon energy sources as a core of the future energy supply. One of such sources is nuclear power. Starting to be a well-affirmed energy source, also nuclear power has to face innovation. In this scenario plays a key role the Generation IV International Forum (GIF) initiative has identified six main designs that will constitute Generation IV reactors. One of these designs is Gas-Cooled Fast Reactors (GFR), of which ALLEGRO reactor should be the first prototype. In order to develop a new design, many studies and investigations need to be done: the following work will be focus on the development of a flow straightener, used to eliminate the flow conditioning, placed at the inlet of a 7 pin ALLEGRO rod bundle and its validation through Particle Image Velocimetry experiments.

## Summary

Abstract.....	3
1. Introduction .....	10
2. Gas cooled Fast Reactor (GFR).....	14
3. ALLEGRO reactor.....	19
3.1 Introduction and designs .....	19
3.2 ALLEGRO core.....	20
3.3 ALLEGRO supporting studies.....	22
3.3.1 CFD investigation of ALLEGRO fuel assemblies .....	22
3.3.2 L-STAR .....	23
3.3.3 ESTHAIR.....	25
3.3.4 PIV experiments .....	26
4. BME Contribution to ALLEGRO Project.....	30
4.1 BME Test Loop and Test Section.....	30
4.2 PIV setup and PIV experiments .....	33
5. Flow straightener investigation .....	36
5.1 Elbow and flow straightener geometry .....	36
5.2 CFD models.....	37
5.2.1 Computational grid .....	38
5.2.2 Grid independence analysis.....	42
5.3 PIV setup and experiments .....	49
5.4 Comparison of the results .....	54
5.5 Phenomenology and unsteadiness of the flow.....	75
5.6 New designs .....	85
6. Summary and conclusion.....	97
References .....	104

## List of figures

FIGURE 1: electricity generation per source from 1990 to 2019 [1] .....	10
FIGURE 2: Scheme of the GFR-2400 MW <sub>th</sub> [4] .....	14
FIGURE 3: One of the modules of Shandong Shidao Bay reactor [6] .....	16
FIGURE 4: ALLEGRO first concept by CEA [7] .....	19
FIGURE 5: ALLEGRO first MOX core [8] .....	21
FIGURE 6: ALLEGRO new refractory pin core [8] .....	21
FIGURE 7: L-STAR loop [10] .....	23
FIGURE 8: Scheme of the heater rod in L-STAR facility [4] .....	24
FIGURE 9: View of the experimental part of the ESTHAIR program [11] .....	26
FIGURE 10: BME test loop .....	31
FIGURE 11: Geometry of BME rod bundle .....	32
FIGURE 12: Modeled geometry (pipe elbow and flow straightener) .....	36
FIGURE 13: 3D CAD of the flow straightener .....	37
FIGURE 14: Geometry details of the grids .....	37
FIGURE 15: Blocking of the lower part of the elbow .....	39
FIGURE 16: Blocking of the change of diameter in the elbow .....	39
FIGURE 17: Blocking of the diffuser .....	40
FIGURE 18: Blocking of the confuser .....	41
FIGURE 19: Blocking of the lamella .....	42
FIGURE 20: Location of the planes .....	45
FIGURE 21: Pressure drop through the flow straightener - Number of elements .....	46
FIGURE 22: Maximum axial velocity in the middle plane - Number of elements .....	47
FIGURE 23: Minimum axial velocity in the middle plane - Number of elements .....	47
FIGURE 24: Average axial velocity in the middle plane - Number of elements .....	48
FIGURE 25: Maximum axial velocity in the outlet plane - Number of elements .....	48
FIGURE 26: Average axial velocity in the outlet plane - Number of elements .....	49
FIGURE 27: Monitoring plan of the PIV experiments .....	50
FIGURE 28: Picture of the PIV setup in BME laboratory .....	51
FIGURE 29: Schematic view of the PIV setup .....	51
FIGURE 30: Axial velocity field for plane 1, PIV experiment output .....	52
FIGURE 31: Monitoring lines .....	53
FIGURE 32: Geometry details about the monitoring lines .....	54
FIGURE 33: Axial velocity profile along Plane1 Line1 .....	55
FIGURE 34: Axial velocity profile along Plane1 Line2 .....	56
FIGURE 35: Axial velocity profile along Plane1 Line3 .....	57
FIGURE 36: Axial velocity profile along Plane1 Line4 .....	58
FIGURE 37: Axial velocity profile along Plane1 Line5 .....	59
FIGURE 38: Axial velocity profile along Plane1 Line6 .....	60
FIGURE 39: Axial velocity profile along Plane1 Line7 .....	61
FIGURE 40: Axial velocity profile along Plane2 Line1 .....	62
FIGURE 41: Axial velocity profile along Plane2 Line2 .....	63

FIGURE 42: Axial velocity profile along Plane2 Line3 .....	64
FIGURE 43: Axial velocity profile along Plane2 Line4 .....	65
FIGURE 44: Axial velocity profile along Plane2 Line5 .....	66
FIGURE 45: Axial velocity profile along Plane2 Line6 .....	67
FIGURE 46: Axial velocity profile along Plane2 Line7 .....	68
FIGURE 47: Axial velocity profile along Plane3 Line1 .....	69
FIGURE 48: Axial velocity profile along Plane3 Line2 .....	70
FIGURE 49: Axial velocity profile along Plane3 Line3 .....	71
FIGURE 50: Axial velocity profile along Plane3 Line4 .....	72
FIGURE 51: Axial velocity profile along Plane3 Line5 .....	73
FIGURE 52: Axial velocity profile along Plane3 Line6 .....	74
FIGURE 53: Axial velocity profile along Plane3 Line7 .....	75
FIGURE 54: Axial velocity field in the elbow, plane 1 .....	76
FIGURE 55: Axial velocity field in the constriction, plane 1 .....	77
FIGURE 56: Axial velocity field in the flow straightener, plane 1 .....	77
FIGURE 57: Axial velocity field in the flow straightener, plane 2 .....	78
FIGURE 58: Axial velocity field in the flow straightener, plane 3 .....	78
FIGURE 59: Lines for the comparison of the velocity profile .....	79
FIGURE 60: Axial velocity profile along a line in the center of the flow straightener .....	80
FIGURE 61: Axial velocity profile along a line at the outlet of the second grid .....	80
FIGURE 62: Axial velocity profile at the outlet of the flow straightener, inlet of the rod bundle .....	81
FIGURE 63: Axial velocity field at 0.114 s, plane 1 .....	82
FIGURE 64: Axial velocity field at 0.8456 s, plane 1 .....	82
FIGURE 65: Axial velocity field at 1.4282 s, plane 1 .....	83
FIGURE 66: Axial velocity field at the outlet plane at 0.2158 s .....	83
FIGURE 67: Axial velocity field at the outlet at 1.3906 s .....	84
FIGURE 68: Axial velocity field at the outlet at 1.918 s .....	84
FIGURE 69: New design 1 .....	86
FIGURE 70: New design 2 .....	87
FIGURE 71: New design 3 .....	88
FIGURE 72: Velocity profile along the line at the outlet for different new designs .....	89

|

|

## 1. Introduction

The 21<sup>st</sup> century is taking to the attention of the whole world on one of the most treating issue, the threat of global warming. Through the use of fossil resources, such as coal and oil, that are easily extractable and provide a high amount of energy, the society has reached a level of wealth as never before. This latter doesn't come without a price: in fact, these fossil fuels produce compounds, such as  $CO_2$ , that are harmful for the humanity and for the environment. With the progress and the born of new economies with a willingness of fast growth, the global demand of energy has increased constantly, as shown in FIGURE 1 for electricity demand.

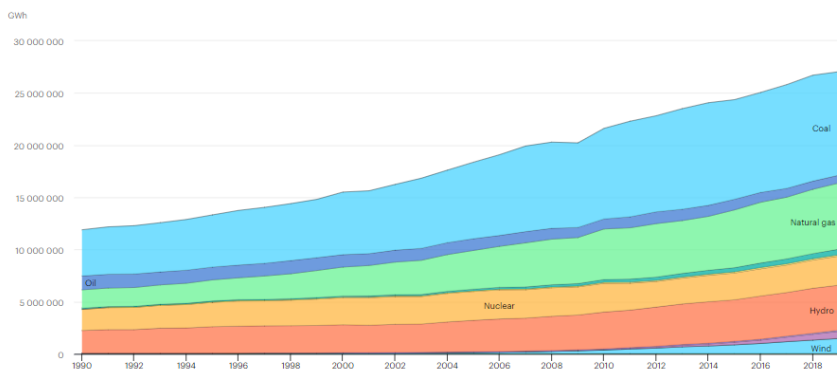


FIGURE 1: electricity generation per source from 1990 to 2019 [1]

For these reasons, the world is currently experiencing an increasing need for development of sustainable, low-carbon energy sources as a core of the future energy supply. One of such sources is nuclear power, obtained by the fission of radioactive elements, such as uranium. Nuclear energy is characterized by extremely low lifetime greenhouse gas emissions and very high capacity factor, especially when compared to other low-emission energy sources: this allow nuclear to contribute to electricity security in a significant way, keeping the grid stable, limiting the seasonal fluctuations in output from renewables and ensuring energy security by reducing dependence on imported fuels [2]. Beside all the benefits of nuclear energy, the prospects for its role remain highly uncertain: some countries have decided to stop investment in new projects and phase out progressively the existing capacity; others see a long-term role for nuclear power in their energy system. These doubts come for many reasons: an aging fleet, the need of a huge initial capital, the risk of construction problems, delays and cost overruns and the possibility of future changes in policy [2]. In addition, there is the ability of nuclear power to compete with other generating technologies on cost, especially in those countries where policies have been introduced for the sustainment of these technologies. Therefore,

Codice campo modificato

Codice campo modificato

Codice campo modificato



the nuclear power can't be seen as a sustainable long-term energy source, unless new, more efficient technologies are introduced. Because of the previously mentioned aging of the current reactor fleet, based on Generation II and Generation III nuclear fission reactors, significant efforts have been made to develop the next, fourth generation. Generation IV is meant to be a large step in the nuclear reactor evolution, with advanced designs that could help to overcome the previously mentioned hurdles. In this scenario plays a key role the Generation IV International Forum (GIF) initiative, created in 2001 to establish an efficient international framework for research and development of Generation IV reactors. To choose the most suitable designs, the GIF has defined four goal areas [3]:

- Sustainability
- Safety and reliability
- Economic competitiveness
- Proliferation resistance and physical protection

Considering these principles, six promising designs on which focus the efforts have been chosen:

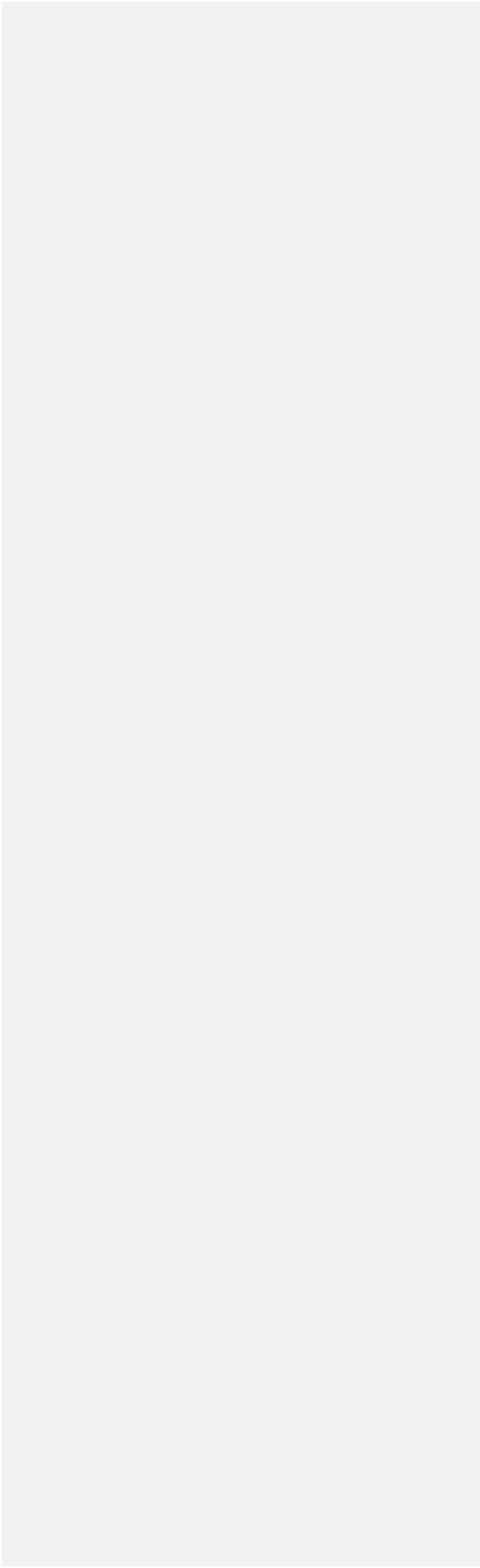
- lead-cooled fast reactor (LFR);
- molten salt reactor (MSR);
- sodium-cooled fast reactor (SFR);
- supercritical-water-cooled reactor (SCWR);
- very-high-temperature reactor (VHTR);
- gas-cooled fast reactor (GFR).

On this latter, of which ALLEGRO reactor should be the first prototype, it will be focused the next chapter, 3.1. In order to develop a new design, many studies and investigations need to be done: some examples regarding the previously made experiments will be done in chapter 3.3. The Budapest University of Technology and Economics (BME) is collaborating in the development of this new design, and a 7 pin ALLEGRO rod bundle experimental loop has been built in the laboratory of the university, as it will be shown in chapter 4. The main goal is to develop a CFD code that would be useful to simulate the thermal-hydraulics behavior of ALLEGRO core. This code should also be validated by means of Particle Image Velocimetry experiments. A starting point for the development of a CFD code, it's to modelling the flow straightener place at the inlet of the 7 pin rod bundle, that it will be needed to eliminate the conditioning of the flow coming from the design of the loop. This investigation, experimental work of this thesis, it will be presented in chapter 5. The outlet results of this CFD investigation will be needed as inlet condition for the CFD model simulating all the rod bundle.

Codice campo modificato

|

|



## 1.2. Gas cooled Fast Reactor (GFR)

The Gas cooled Fast Reactor (GFR) is one of the six reactor concepts developed in the context of the Generation IV International Forum (GIF).

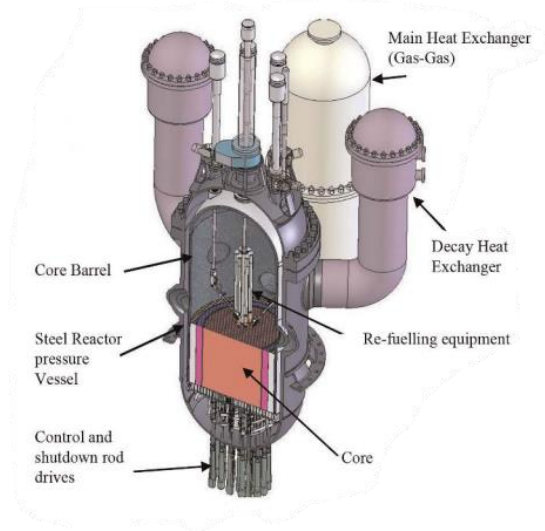


FIGURE 2: Scheme of the GFR-2400 MW<sub>th</sub> [4]

GIF is a cooperation between different countries with the common goal to carry out the research and the development needed to establish the feasibility of the new generation of reactors. In particular, the main aspect that is taken in consideration for all the designs is the possibility to have a sustainable closed fuel cycle. Regarding the GFR, this is possible thanks to the fast neutron spectrum, that permits a much better utilization of the fissile material and a reduction of the most dangerous part of the nuclear waste, the actinides, through transmutation. Combined with this aspect there is the advantage to use high output temperature coolant (up to 850 °C), that allows targeting high energy conversion efficiency (43-45%) thanks to a direct connection with a gas turbine, building up a highly efficient closed Brayton cycle, and opens possibilities to new applications of nuclear energy, such as heat production that can be used for different applications from metallurgy to hydrogen or synthetic hydrocarbon fuel production [5]. In addition, helium as coolant represents a good solution regarding:

- Safety, since it doesn't have a threshold effect due to phase changing, reducing the potential of reactivity swings under accidental conditions; it has very limited voiding reactivity effects;

Codice campo modificato

Codice campo modificato

ha formattato: Tipo di carattere: Non eseguire controllo ortografia o grammatica

it is compatible with water and in general it has good compatibility with all the structural materials; it has a low activation.

- Operational activities, since its optical transparency allows in-service inspection.
- The previous knowledge of the element, well known and used for many different applications.

No GFR has ever been build, but the target is a 2400 MW<sub>th</sub> commercial electricity generating reactor. The GFR-2400, in such way is called this reactor, will have a reactor core located in a steel pressure vessel, surrounded by the main heat exchanger, that is supposed to be gas-gas heat exchanger, and the decay heat removal loops. Control and shutdown rods will be inserted from the bottom of the reactor, in order to minimize theirs heat loads. Inside the reactor pressure vessel above the core an innovative fuel handling equipment is situated.

Main issues in the GFR are the high-power density (100 MW/m<sup>3</sup>) and the lack of the thermal inertia of the coolant. Considering these aspects, the key challenges related to the development of the GFR are:

- An innovative refractory fuel, that must be able to withstand high temperatures
- Demonstration of the safety and reliability of the safety systems to cool down the core in every situation.

To develop the necessary technologies such as fuel, fuel assemblies, helium related technologies and safety systems, and prove the feasibility of the GFR, an experimental reactor of 75 MW<sub>th</sub> power (ALLEGRO) is planned to be built.

[In addition to the experience that will be gained with ALLEGRO reactor, also the one coming from the Shandong Shidao Bay 200 MW<sub>e</sub> High-Temperature Gas-Cooled Reactor Pebble-Bed Module \(HTR-PM\) Demonstration Power Plant could be used. Basing on the experience gained with the 1990s test reactor HTR-10, Chinese Government continued investing in High-Temperature Gas-Cooled Reactors, with the choice in 2006 to make HTR-PM a key national governmental R&D project. Before the construction, starting from 2010, preliminary studies have been carried out in an Engineering Lab with a 10 MW helium test loop, regarding the helium circulator; the fuel handling system; the control rod driving system; the fuel, with small absorber balls system; the steam generator, made of helical heat transfer tube bundles; and the helium purification system. In 2015 the civil work of the nuclear island ended, making the component installation starting. In July 2020 there was the commissioning of the rector, of which the first connection to the grid was made in 2021. The reactor consists of two pebble-bed reactor modules coupled with a 210 MW steam turbine. Each reactor module includes a reactor pressure vessel, a graphite, carbon, and metallic reactor internals, a steam](#)

generator, and a main helium blower. Each module, shown in FIGURE 3, has a thermal power of 250 MW<sub>th</sub>. The helium temperatures at the core inlet and outlet are respectively 250 °C and 270 °C.

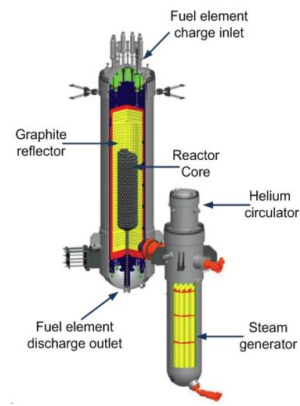


FIGURE 3: One of the modules of Shandong Shidao Bay reactor [6]

Many studies and experiments have been done in several years, allowing the construction of an innovative reactor such as HTR-PM. All this experience could be used, especially regarding the helium management and the safety of such technology, in the construction of ALLEGRO and, consequently, of the first GFR.

## 2.3. ALLEGRO reactor

### 2.13.1 Introduction and designs

The idea of the developing of a He-cooled fast reactor goes back to '50/'60. The first concept, named ALLEGRO, was a 75 MW<sub>th</sub> experimental reactor proposed by CEA in 2009. It consists of a smaller scale version of the GFR-2400 made by two He loops that remove the heat from the core connected to two main heat exchangers with pressurized water on the secondary side. This option makes it possible to rely on basic water-helium technology and relatively low temperature materials, even in case of high outlet temperature of the coolant. Heat is finally transferred by air coolers from the second loops to the atmosphere, as final heat sink. In order to investigate the gas-gas heat transfer that will be used in GFR-2400, two additional prototype heat exchangers are added. In addition, there are three Decay Heat Removal (DHR) loops operating under forced gas circulation and potentially under natural circulation in some occasions. It was characterized by two different cores: a first one, using MOX, and a second refractory one, that could reach higher temperatures. This first design, shown in FIGURE 4, became the reference one for the GFRs.

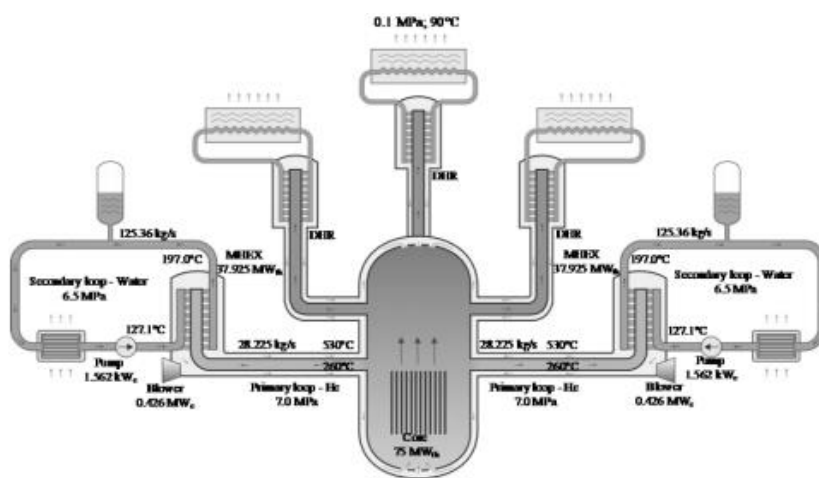


FIGURE 4: ALLEGRO first concept by CEA [7]

In 2010 four nuclear research institutes and companies of the Visegrad-4 region (ÚJV Řež, a.s. - Czech Republic, MTA EK - Hungary, NCBJ - Poland, VUJE, a.s. - Slovak Republic) decided to start joint preparations aiming at the construction and operation of the demonstrator (ALLEGRO) of the concept of Generation IV gas-cooled fast reactor (GFR) based on a Memorandum of Understanding signed in 2010. In order to study safety and design issues and also the medium and long-term governance and

Codice campo modificato

Codice campo modificato

financial issues, the four aforementioned organizations created in July 2013 a legal entity, the “V4G4 Centre of Excellence”, which performed the preparatory works needed to launch the ALLEGRO Project. Therefore in 2015 the ALLEGRO Project was launched, with a precise design and safety roadmap where all the institutes have their own specialization. The ALLEGRO V4G4 design is almost the same as the CEA one, with some changes. A UOX fuel is under investigation as first core, since MOX fuel would involve several legal issues related to proliferation. To increase safety, a new concept of active-passive DHR system is under development too.

For the moment is being agreed that the ALLEGRO project will be divided in two phases: a preparatory phase (2015-2025) and a realization phase (after 2025). During this preparatory phase the main technical challenges that then will be a fundamental part for the development of GFR-2400, are the fuel handling machine, the decay heat exchangers, the helium purification technologies, and the new refractory core.

#### 2.23.2 ALLEGRO core

During its life, ALLEGRO reactor will have different cores. The core of a nuclear reactor is made by many rod bundles called assemblies, made by a plurality of fuel rods arranged in a lattice-like configuration. Fuel spacers, that could have many different designs, are placed along the rod bundles in order to keep them away from each other. At the beginning, MOX (Mixed Oxide, (U, Pu)O<sub>2</sub>) (or maybe UOX) fuel pellets, with 15-15Ti steel cladding and wire spaced pin type bundles, which are helically wrapped wires around the pin along its axis, already developed for Sodium Fast Reactors, will be used. The wire spacing is used both to maintain a constant spacing between the fuel pins and to enhance the turbulence and so the heat transfer. Due to the metallic nature of the cladding, the MOX core must be operated under moderate core outlet temperature (530 °C). In addition to the MOX assemblies, inside the first core there will be also six experimental assemblies to investigate the new refractory core. These experimental assemblies will be in the center of the core, where the neutron flux is flat, and at the boundaries, where the neutron flux sees a gradient, in order to analyze different behaviors.

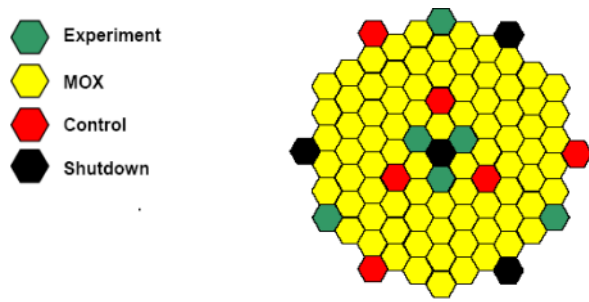


FIGURE 5: ALLEGRO first MOX core [8]

Codice campo modificato

Codice campo modificato

In a second stage, a ceramic core will be used, with U-Pu carbide pellets. Two different designs were considered at first: the plate core, where the plate type fuel elements are arranged within a basket made of  $\text{SiC}_f/\text{SiC}$ ; the pin core, similar to the MOX core, but with (U, Pu)C fuel pellets inside  $\text{SiC}_f/\text{SiC}$  cladding and with the implication of grid spacers instead of the wire ones. This latter was the chosen one [as design for the ALLEGRO core](#). This core is supposed to reach outlet temperatures up to 850 °C, being a good test for the GFR core. Due to the high temperatures reached, both materials and thermal-hydraulics conditions in the core must be known deeply. This aspect has been investigated, and it is currently under investigation, with the help of Computational Fluid Dynamics (CFD) models, experimental facilities, such as L-STAR, and projects, such as ESTHAIR, FP7 GoFastR and FP7 THINS. All these tools will be analyzed in the next section in order to provide some tangible examples of the work that has been carried and the obtained results.

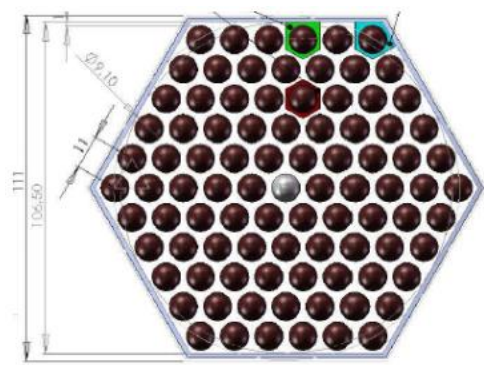


FIGURE 6: ALLEGRO new refractory pin core [8]



### 2.33.3 ALLEGRO supporting studies

#### 2.3.13.3.1 CFD investigation of ALLEGRO fuel assemblies

To simulate the thermal-hydraulic behavior of the coolant inside ALLEGRO fuel assemblies, Computational Fluid Dynamic (CFD) simulations have been developed both for the MOX and the ceramic rod bundles [9]. The model of the MOX rod bundles of the starting core contains six subchannels with the fuel rods and the spiral wire spacers. For the ceramic rod bundles, a 60-degree segment model has been developed, involving the honeycomb grid spacers. In both cases a mesh analysis has been done to choose the right parameters that optimize the precision of the results and the computational cost. In the simulations, the goal was to analyze mainly the velocity and the distribution of the temperature along the rods.

About the MOX rod bundles, the velocity distribution is the same in the middle and at the end of the active bundle, with a rotation due to the wires. The velocity is lower close to the rods and to the wire due to the wall effect and increases about 70% along the bundle due to the change in density, consequentially at the heating of the coolant. A cross flow is present due to the wires, that enhance the mixing of the coolant. It increases along the bundle too. The temperature is higher near the wall due to the boundary layer effect and near the wire due to rib effect. Where the fluid velocity is lower, the temperature is higher. The importance to model the solid part (the cladding and the wire material) has been shown, otherwise a significant overestimation of the rod surface would be present. Dittus-Boelter correlation is used to compute the heat transfer coefficient, but the results don't match the ones from the simulations, maybe due to the enhancement of the mixing and so of the heat transfer due to the wires.

Regarding the CFD simulation of the ceramic rod bundles, the velocity profile is characterized at the inlet by a fully developed field, while at the outlet it's more inhomogeneous due to the uppermost spacer grid. No differences between subchannels of the same type are underlined, but large difference between different types are present: outlet velocity and mass flow rate are lower in the corner because of small section and large hydraulic resistance. The velocity increases due to the decrease of the density, as it was seen in the MOX rod bundles, and the magnitude is the same of the MOX core. The cross-sectional velocity is more evident near the spacer due to eddies and enhanced coolant mixing. The coolant mixing is less intensive than in the MOX core. The difference of temperature between the rod walls and the coolant is bigger than in the MOX core. As there was a difference between the mass flow rate and the outlet velocity between different types of channels, the same difference can be seen in the temperature, where in the corners the temperature is 250°C more than average one. This

ha formattato: Tipo di carattere: Non eseguire controllo ortografia o grammatica

Commentato [OGI1]: T= temperature?

temperature has to be reduced for safety reasons: we can lower the Pu content in the corners or use vanes on the spacers to intensify the mixing. As in the previous case, there is the necessity to model the cladding material and the wire material, in order not to overestimate the temperature. The heat transfer coefficient fits well the Rehme correlation, with a difference caused by the spacer grids.

The obtained results represent approximately the real behavior that the coolant will have in ALLEGRO subassemblies. However, in order to strengthen the reliability of the results, the CFD model could be validated using some experimental data. An example of this process will be made in the next section, where the L-STAR facility is taken into consideration.

#### 2.3.23.3.2 L-STAR

Within the framework of the European FP7 GoFastR and THIS (Thermal Hydraulics of Innovative Nuclear Systems) projects, the L-STAR facility, shown in FIGURE 7, has been built at Karlsruhe Institute of Technology. It is devoted to the collection of experimental data regarding a single rod cooling using pressurized gas under a wide range of conditions. These data are useful to create and validate CFD models that can be used in the thermal-hydraulic design of the ALLEGRO core.

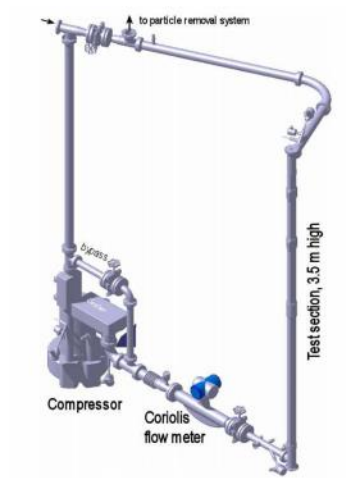


FIGURE 7: L-STAR loop [10]

The L-STAR loop allows examining the flow regimes (both turbulent and laminar) and the heat transfer from the rod to the cooling fluid, that may be  $N_2$ ,  $CO_2$  or air. The test section is a 3246 mm long hexagonal flow channel, that contains the cylindrical heated rod, scaled and designed to describe a complete subchannel around a single GFR rod. The maximum temperature that can be reached is 200 °C and the maximum operating absolute pressure is 0.3 MPa. The heating

Codice campo modificato

Codice campo modificato

power of the rod, as well as the mass flow rate, can be adjusted to simulate different scenarios. The rod consists of four different concentric layers, as shown in FIGURE 8: the innermost part is a ceramic support made from compressed MgO powder that is used as insulation. The next layer is made by a NiCr8020 resistive material wires, embedded in ceramic glue to fix them to the ceramic filler, used to fill up the gap between the ceramic support and the heater shell with thermocouples. The heating layer is 2500 mm long, made by six individual heating elements, each 407 mm long, with 10 mm gap between them. The outermost layer is the cladding shell, made of stainless steel.

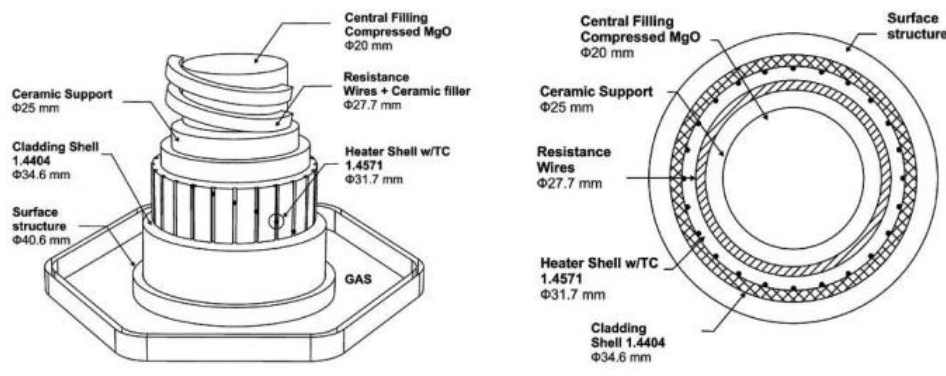


*FIGURE 8: Scheme of the heater rod in L-STAR facility [4]*

The test section is equipped with two optical windows, which allow access for optical flow measurement methods. For velocity measurements, Laser-Doppler Anemometry (LDA) was applied. This system was developed at TU Dresden and enables the simultaneous measurement of particle velocities and relative position of the individual particle trajectories within the measurement volume. Additional experiments with a ribbed rod surface, made with metallic rings, were carried out to analyze the heat transfer enhancement.

Several CFD models have been made during these years. Kubačka J. et al. (2013) have performed some experiments using CFD code Ansys FLUENT for both the smooth surface heated rod and the artificial surface texture heated rod, both in transient and steady-state cases. Performed calculations were focused in detail on the evaluation of the various flow regimes, considering the resistance coefficient. The results showed a good conformity between the experimental data and the simulations one for high Reynolds numbers, due to the application of the k-ε turbulence

model. On the other hand, less precise results were shown for flows with low Reynolds numbers. This difference was said to be due to the quality of the mesh and to the turbulence model used. Further investigations regarding these aspects were underlined to be needed.

Simulations have been carried out by S. Tóth et al. (2020) recently. This analysis was focused especially on the mesh sensitivity: it was clear the necessity to model the structural elements, considering the thermal conduction, and the heat radiation. Different models were used, and the SST k- $\omega$  turbulence model shown up to be the one to give results with smaller deviation. The results regarding the rod surface temperature were in general improved, but there were still some cases where the deviation between the simulation and the experiment was significant. This was imputed to the turbulent heat transfer and its link to the turbulent Prandtl number. Each turbulence models handle the turbulent Prandtl number differently. In the ANSYS CFX code, the one used for this simulation, the default value is 0.9. Further investigations changing turbulent Prandtl number are needed to find the most precise empiric correlation.

The same result regarding the influence of the turbulent Prandtl number was found in the framework of THINS project. Different simulations were done using different turbulence approaches based on RANS (Reynolds-Averaged Navier-Stokes), SAS (Scale Adaptive Simulation) and ZLES (Zonal Large Eddy Simulation). These two latter models are used for finer resolution simulations. Nevertheless, the same discrepancies in the temperature distribution were found out, and additional works will be necessary.

#### 2.3.33.3.3 ESTHAIR

The ESTHAIR program has the objective to validate some thermal-hydraulic aspects, mainly the correlations on the pressure loss and on the heat exchange coefficients within the core sub-assemblies, between the fuel pin and the helium coolant [11]. In GFRs, the variation of the gas transport properties, due to high temperature gradient, is a recurrent problem. The consequence is a distortion of the velocity profile that impacts on the pressure drop and the heat coefficient. The use of standard correlations such as Dittus-Boelter for turbulent flow and Poiseuille for laminar flow, that don't take into account the difference between the bulk and the surface temperature, leads to an underestimation of the fuel wall temperature and of the core pressure loss. New more precise correlations must be found. This program was supported by two different parts: on the one hand an experimental air test section shown in FIGURE 9 was used, performing tests in non-heating and heating conditions with Reynolds numbers similar to the ones we have in ALLEGRO; on the other hand, a numerical simulation program based on a simplified modelling of the ESTHAIR sub-assembly was performed.

ha formattato: Tipo di carattere: Non eseguire controllo ortografia o grammatica

ha formattato: Tipo di carattere: 9 pt, Colore carattere: Testo 2

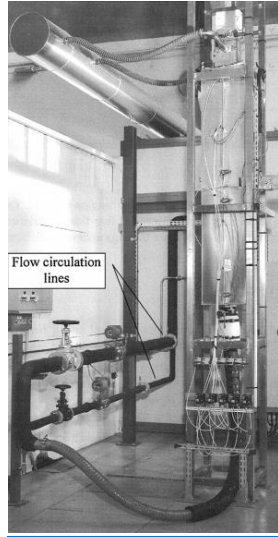


FIGURE 9: View of the experimental part of the ESTHAIR program [11]

For the first, the experimental data were compared with the correlations to understand which one represent better the flow behavior. Regarding the friction factor, the Rehme correlation correctly reproduces the experimental data over the entire Reynolds number range of tests, with a slightly less precision for lower Re. The same result about this correlation was found in the CFD investigation of ALLEGRO assemblies. Regarding the heat transfer, the McEligot and the Baxi correlations show the best results, but still a 15% overestimation of the Nusselt number is present. The instabilities are present especially at the low Reynolds regimes, and so further investigations are required for these conditions. In numerical simulations the results match the ones of the experiment, both for the pressure drop and the heat transfer, and generally are better than the values given by the correlations.

#### 2.3.43.3.4 PIV experiments

The Particle Image Velocimetry (PIV) experiments are not strictly related to the development of ALLEGRO reactor, but they give a set of experimental data that can be used for the validation of the CFD models. To perform these experiments, seeding particles are added to the flow that is investigated. It's important that these particles respect some characteristics, such as small diameter and low specific gravity, so that they don't impact in the behavior of the coolant. The coolant is forced to pass inside a test section, with a design that respect the situation that we want to study (for example 5x5 rod bundle with spacer grids). In order to be allowed to carry out optical flow studies of the test section, it's fundamental that its index of refraction matches the one of the working fluids.

Codice campo modificato

Codice campo modificato

When the light passes through materials with different indexes of refraction, it bends at the interface of the materials causing distortion or hidden areas. However, by matching the index of refraction, the bending of light is eliminated or minimized, making the test section optically transparent and allowing PIV experiments [even within complicated geometries](#). It is possible then to use high speed cameras to capture the flow behavior and full velocity fields can be obtained, showing the turbulence evolution.

High-fidelity PIV measurements can be achieved performing a massive sensitivity analysis. The goal of this analysis is the elimination of systematic errors. The systematic error can be induced by peak locking, particle slip, refractive index difference, perspective effect and local displacement variation. The dominating ones are the perspective angle error and the local displacement variation error. The random error can be induced by interrogation algorithm, particle image density, particle image diameter, image noise and out-of-plane motion. This latter is recognized as the main cause. In order to decrease these errors and have better results than the one obtained previously, in the high-fidelity approach the lateral image displacement is realized by employing a long focal length lens and setting a large magnification ratio.

Even more precise data can be obtained using Time Resolved PIV (TR-PIV). A clearer picture of the flow can be seen by capturing a series of velocity fields that are correlated to each other in time. Typically, this means that the same fluid structure can be seen in multiple consecutive velocity fields. The data is often analyzed by watching an animation of the velocity fields, so that the viewer can see how fluid structures move from frame to frame and how they are interacting over time.

#### 4. BME Contribution to ALLEGRO Project

At Budapest University of Economics and Technology, in the framework of EU SafeG Project, a test loop for the hydraulics study of 7 pin ALLEGRO rod bundle has been build and is currently under investigation. The goal is to develop CFD models and validate them thanks to experimental data coming from PIV experiments carried out on the same test section. In the following sections the test loop and the PIV setup will be explained, in order to give a good background overview of experimental part.

##### 2.44.1 BME Test Loop and Test Section

The construction of the test loop at BME, shown in FIGURE 10, started in October 2020. The goal, as previously said, is to investigate the hydraulic behavior of a 7 pin ALLEGRO rod bundle using water as coolant and not helium as it will be in ALLEGRO. This solution makes the measurements and the management of the coolant easier and more affordable ; the obtained results are valid also for the ALLEGRO case, thanks to the fact that the flows have the same Reynolds number range. In fact, beside the fact that the value of the velocity is different in the two cases, if the flows have the same shape of the velocity profile and the same degree of turbulence, the modelling solution of one flow will be also suitable for the other. Therefore, the Reynolds number in BME test loop is adjustable between  $\sim 0$  and 80000, including the range  $\sim 16000 - 20000$  that is significant for the ALLEGRO refractory core.

The water is coming from the tap, and in order to prevent the residuals and other particles from damaging the test loop and from falsifying the results of the PIV measurements, two different filters are used. The coolant is then put in an open water tank, where the loop starts and ends. The circulation of the coolant is provided by a centrifugal pump, and the flow rate can be set thanks to an ultrasonic flow meter. Due to the fact that the centrifugal pump, being in function for hours, could heat up the coolant, changing the properties and making the CFD simulations harder, a heat exchanger water-water has been included. The coolant flows then through some elbows and goes to a flow straightener, which is useful to eliminate the velocity field conditioning due to the elbow and balance the inlet conditions of the test section, giving a more homogeneous velocity field. The function of the flow straightener, its modelling and the validation of this model will be subjects of a more detailed study in the following section. After the flow straightener, the coolant goes in test section, and the end of which, thanks to a T junction, it goes back to the tank.

Commentato [OGI2]: Water-water heat exchanger

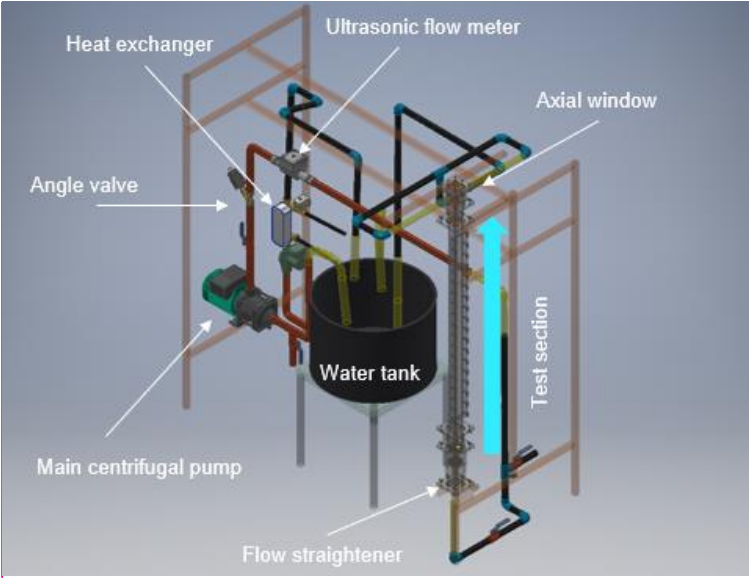


FIGURE 10: BME test loop

The test section is made by 1-meter-long vertical rod bundle with 7 rods and 4 spacer grids. Different spacer grids, with different solutions of mixing vanes, have been designed in order to influence the hydraulic behavior of the coolant, and the current most indicated solution was found in the spacers with twisted vanes. The geometry, as reported in [Table 1](#) and can be seen in [FIGURE 11](#), is upscaled to meet the same hydraulic conditions than in ALLEGRO.

Table 1: Comparison with the geometry details of ALLEGRO assembly and BME test section

	ALLEGRO assembly	BME test section
Diameter of the rods [mm]	9.1	10
Height of the spacer grids [mm]	26	28
Distance between the spacers [mm]	246	293

Formattato: Interlinea: multipla 1.3 ri

Formattato: Interlinea: multipla 1.3 ri

Formattato: Interlinea: multipla 1.3 ri

Formattato: Interlinea: multipla 1.3 ri

Formattato: Interlinea: multipla 1.3 ri



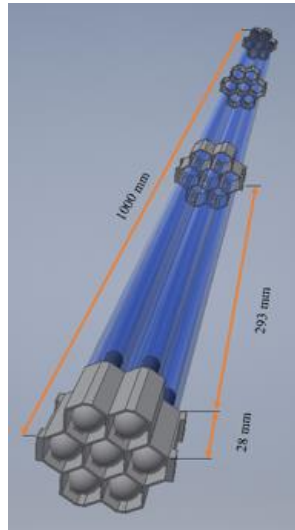


FIGURE 11: Geometry of BME rod bundle

Regarding the materials, on one hand, the rods are made of FEP (Fluorinated Ethylene Propylene); this allows to match the Index of Refraction of water, making the PIV experiments successful; on the other hand, the other components (like the pipe) are made of Acrylic: in this case the Index of Refraction is not matched, but it doesn't create an issue since the Acrylic in this case the Index of Refraction is not matched, but it doesn't create an issue since the Acrylic parts are not curved surface and therefore they do not distort the image.

The flow characteristics are summarized in [Table 2](#). The volumetric flow rate is set to 6 m<sup>3</sup>/h and is maintained under control thanks to the ultrasonic flow meter. The temperature of the water is 30°C and is maintained constant thanks to the heat exchanger. The pressure of the water can be considered to be the atmospheric one at the outlet, since the water is discharged in an open water tank. The properties of the water, such as density and dynamic viscosity, are computed considering the previously mentioned conditions and the mass flow rate can be computed considering these properties.

Table 2: Flow characteristics in BME test loop

	Volumetric flow rate [m <sup>3</sup> /h]	Temperature [°C]	Pressure [bar]	Density [kg/m <sup>3</sup> ]	Dynamic viscosity [Pas]	Mass flow rate [kg/s]

Formattato: Interlinea: multipla 1.3 ri

Value	6	30	1	995,6515	7,9735 E-4	1,6594
-------	---	----	---	----------	------------	--------

#### 2.54.2 PIV setup and PIV experiments

To provide experimental data for the validation of the CFD codes, the test loop is provided with a PIV equipment. It consists on a laser connected to a power supply, with a beam guide arm and a beam forming optics that allow to carry out the experiments in different sections of the test section. The camera and the laser are connected to a computer, where [the software](#) Dantec DynamicStudio is used.

The main components of the setup are:

- tracer particles made by polyamide spheres (in order to match the index of refraction) with average diameter of 50  $\mu\text{m}$
- Laser source: Litron Nano L PIV dual Nd: YAG laser (maximal impulse energy: 135 mJ, wavelength: 532 nm, pulse length:  $\sim 6$  ns, maximum flash frequency: 15 Hz)
- Beam guide arm and beam forming optics
- SpeedSense Lab 110 high speed digital camera, resolution: 1 megapixel (1280x800 image recording frequency: 1690 fps, puffer: 12GB
- Lens: Nikon AF Micro-Nikkor 60mm f/2.8D
- Imaging Synchronization Devices: Dantec Timer Box (80N77)
- Synchronization, image capture and image processing software: Dantec DynamicStudio, newest version: 6.11
- Camera and beam optics mounting tripod systems

Ideally, the frequency resolution that would be liked to be achieved is 10-20 kHz, but due lack of budget the resolution of the camera is currently limited at 1690 fps. Due to this resolution the frequency laser could be 1500-2000 Hz.

~~For each PIV measurement 2000 pictures. After the acquisition of the pictures, some processes are carried out on Dantec DynamicStudio to eliminate the pictures that due to some reflection problems are not reliable. A mask is created to consider only the area of interest. The pic of velocity that seem to be impossible and might be coming from some measurement errors are eliminated and the average velocity field is then computed. In flow straightener measurements, 2000 image pairs were recorded in the vicinity of the straightener grids. Each gap of the compartment grid was examined. The first 100 image pair were discarded from the 2000 images captured because the lasers have a "warm-up" time requirement; therefore, the quality of the images at the beginning of the acquisition is not good. To get a sufficiently detailed picture of the flow field, post-processing of the raw images~~

Formattato: Interlinea: multipla 1.3 ri

Formattato: Interlinea: multipla 1.3 ri

Formattato: Interlinea: multipla 1.3 ri; Struttura + Livello:2 + Stile numerazione: 1, 2, 3, ... + Comincia da:1 + Allineamento: A sinistra + Allinea a: 0.25" + Imposta un rientro di: 0.52"

Formattato: Interlinea: multipla 1.3 ri

is necessary. In the first step, an average image of 1900 image pairs was created. This average image was extracted from each image to reduce the effect of the elements that are present in each image (shadows, glitches and static elements). Laser light is not uniform in intensity along the length of the illuminated plane. Since not all static elements can be eliminated from the images in this way, the static parts and regions not included in the flow field have to be masked out with digital masks. After these steps, the individual image pairs were used to create the instantaneous vector fields separately. From these 1900 vector diagrams, the time-averaged vector field describing the region after the spacer was created. With this method, not only the time-averaged velocities can be obtained, but also an estimate of the temporal fluctuations of the velocity vectors.

## 5. Flow straightener investigation

As said in the previous sections, the installation of a flow straightener has been necessary in order to eliminate the conditioning coming from the elbow and to balance the inlet conditions of the test section giving a more homogeneous velocity field. My work was focused on the developing of a CFD model that could simulate the behavior of the fluid in the flow straightener, validating then it by means of the PIV experiments. In the following sections the description of the geometry of the flow straightener, the mesh modelling and the CFD simulations, the PIV experiments and the comparison between the results will be presented.

### 2.65.1 Elbow and flow straightener geometry

The geometry that has been modeled is shown in [FIGURE 12](#). The lower part is made of the pipe elbow, after which there is a restriction of the diameter and then the flow straightener.

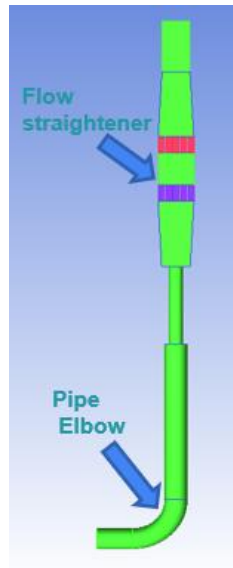


FIGURE 12: Modeled geometry (pipe elbow and flow straightener)

The geometry of the flow straightener was carefully developed in order to eliminate any conditioning coming from the elbow. The coolant, coming from the elbow, enters in the first part of the flow straightener, the diffuser, that thanks to the increase of the area reaching a section of 50x50 mm, reduces the velocity. The following section is composed by the lamella: there are two grids with 5x5 square channels with 4.8 mm edge and 25 mm height, separated by lamella of 2 mm thickness. These are useful to break the conditioning of the flow. The last part is made by a confuser, where the velocity of the flow is increased again thanks to the reduction of the area. In [FIGURE 13](#) the 3D CAD of the flow straightener, with some geometry details, can be seen, while in [FIGURE 14](#) geometry information regarding the grids are presented.

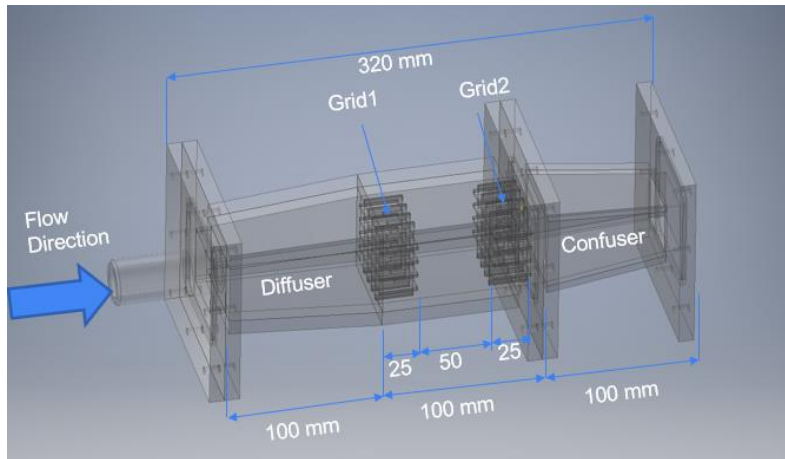


FIGURE 13: 3D CAD of the flow straightener

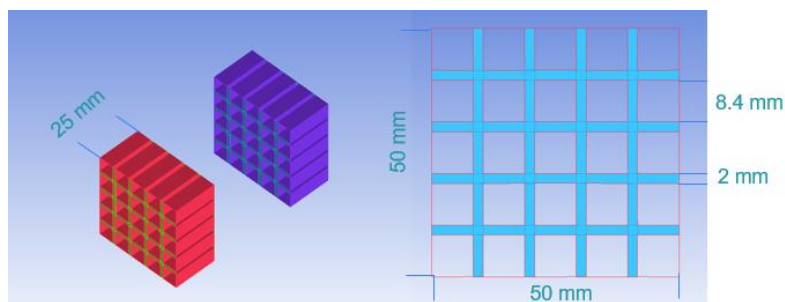


FIGURE 14: Geometry details of the grids

## 5.2 CFD models

For the CFD investigations the grids have been performed using ICEM CFD 19.2, while the simulations have been carried out with CFX 19.2

### 2.7.15.2.1 Computational grid

At the base of the developing of a CFD code there is for sure the choice of a proper computational grid, that must satisfy the requested precision of the results. This precision will be evaluated in the following section by means of a grid independence study. In this case the computational grid was computed using a multiblock approach using ICEM CFD 19.2, that allows to refine the mesh in the

regions next to the wall, to have a better description of the gradient of the velocity and allows to have a better discretization of the lamella part too. The mesh is computed using hexahedra volume cells.

Since the dimension of the domain was quite important, it was divided in different parts and modelled separately. The parts were: the lower elbow; the lower part of the flow straightener, corresponding to the diffuser; the grids, that have been modelled separately, but with the same parameters; the upper part of the flow straightener, corresponding to the confuser. The lower elbow is defined by four different main blocks: three of them are useful to describe the lower part of the elbow, where there is the curve, as shown in [FIGURE 15](#), and one is used for the last part of the elbow where the diameter is smaller. In addition two small blocks have been created in where there is a change of diameter, as can be seen in [FIGURE 16](#), so to have more elements in this section to better describe the behavior of the fluid, without increasing the number of the elements in the straight direction, where it wouldn't be useful. O-grid is present in the circular section of the pipe, to have a better description of the flow near the wall.

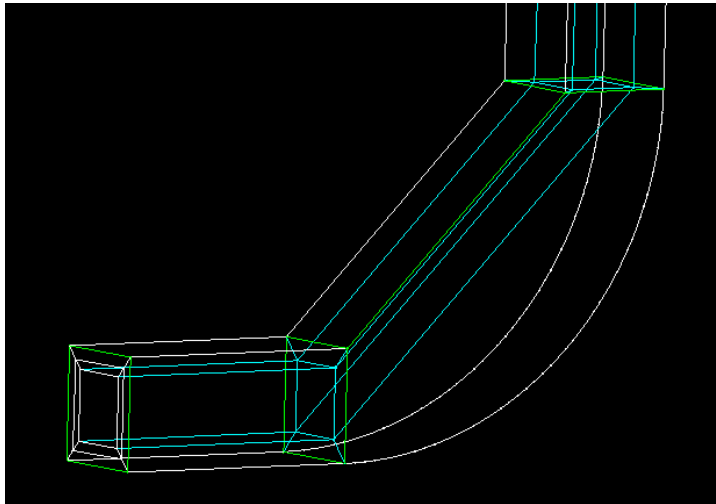


*FIGURE 15: Blocking of the lower part of the elbow*

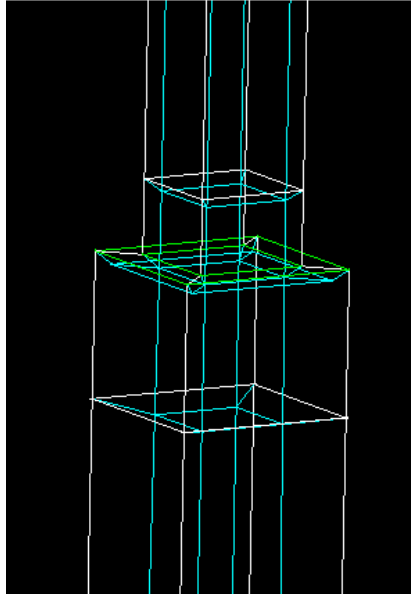


FIGURE 16: Blocking of the change of diameter in the elbow

The blocking of the diffuser and the confuser is shown respectively in [FIGURE 17](#) and [FIGURE 18](#). Regarding the diffuser, a small part of the pipe coming from the elbow has been included so that the change of diameter is better modeled. O-grid is present in the circular pipe for the same reason that was previously explained. In the confuser there are two main blocks, and the refinement near the wall is made increasing the density of the nodes going nearer the wall and decreasing the density in the center of the edge. This approach will be used for the modelling of all the rectangular pipes, as it will be seen in the description of the lamella.

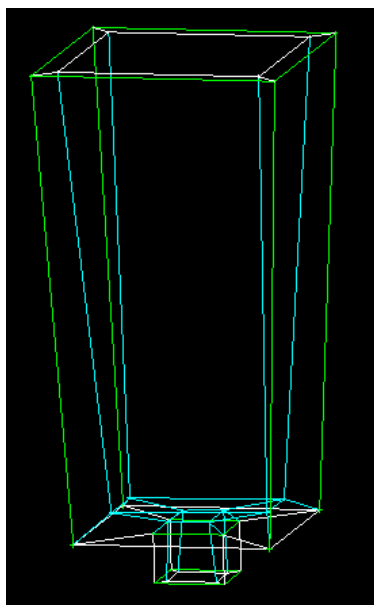


FIGURE 17: Blocking of the diffuser



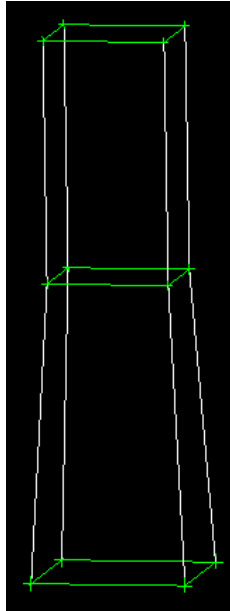


FIGURE 18: Blocking of the confuser

For the grid part, at each channel is associated a block, as shown in [FIGURE 19](#), and the number of nodes it's increasing next to the wall since it's most interesting part from the hydraulic point of view and it's the one that need a better modelling. The blocks between the channels, where there is the solid part of the lamella, have been eliminated and this part is not modelled, since the experiment is carried out in adiabatic conditions and the conduction heat transfer hasn't been considered. |

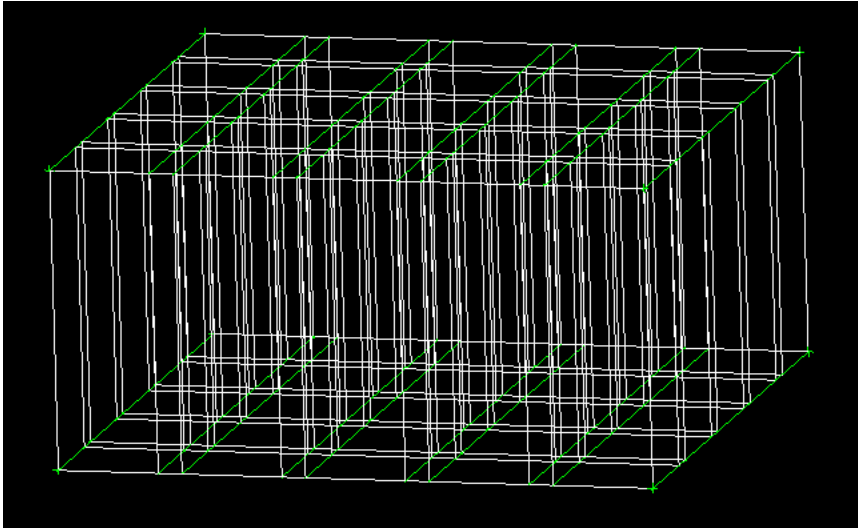


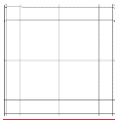
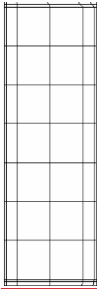
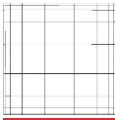
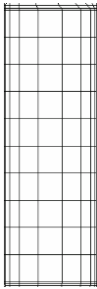
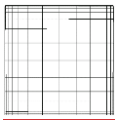
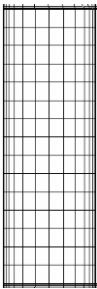
FIGURE 19: Blocking of the lamella

In this section only the general method used for the modelling has been explained, without explaining the number of nodes and elements that have been used. This matter will be discussed in [5.2.2](#), where different grids will be explained and, by means of a grid independence study, the best one will be chosen to carry on the analysis.

#### [2.7.25.2.2](#) Grid independence analysis

The grid independence analysis aims to demonstrate that over a certain level of refinement the result is not going to be influenced by the grid itself and so is basically the way in which it is possible to be sure that the analysis performed is providing results with a proper accuracy. In order to get the grid independence analysis, simulations of the very same physical problem with different grid refinements have to be performed in order to estimate the order of convergence of the system. All the simulations have been carried out with CFX 19.2, using SST k- $\omega$  turbulence model in steady state condition. Other turbulence model will be investigated in the following section, when the most convenient mesh will be chosen. For all the simulations the boundary conditions are the same described in [Table 2](#). At the wall no slip condition has been imposed, in addition to the smooth one. In [Table 3](#) are reported the details about the number of nodes, [the](#) elements of the different meshes [and some close-up of the section of the lamella and the channel of the lamella, in order to show the refinement also from a tangible point of view](#). The different meshes have been obtained starting from the coarse one and then changing the number of the nodes both in the section direction and in the streamwise direction, thanks to the rescaling tool available for the blocking meshes. Processing the results has been made using [MATLAB](#).

Table 3: Parameters of the different meshes

	# nodes	# elements	Section mesh of the channel of the lamella Pictures	Streamwise mesh of the channel of the lamella
M1	122_169	106_629		
M2	398_752	364_226		
M3	1_328_828	1_250_717		

Formattato: Interlinea: multipla 1.3 ri

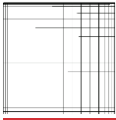
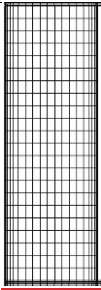
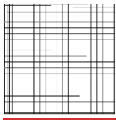
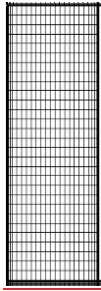
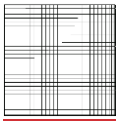
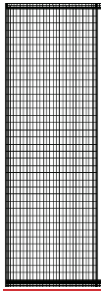
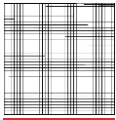
Tabella formattata

ha formattato: Non Evidenziato

Formattato: Interlinea: multipla 1.3 ri

Formattato: Interlinea: multipla 1.3 ri

Formattato: Interlinea: multipla 1.3 ri

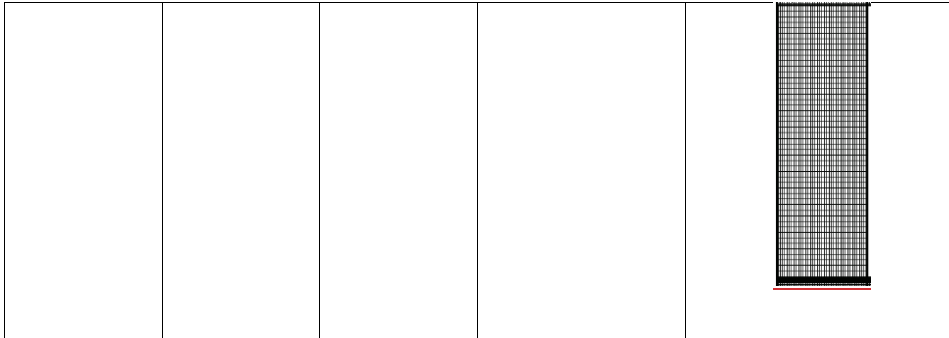
M4	4_439_828	4_264_726		
M5	12_273_706	11_944_709		
M6	35_678_774	35_050_694		
M7	78_772_471	77_704_983		

Formattato: Interlinea: multipla 1.3 ri

Formattato: Interlinea: multipla 1.3 ri

Formattato: Interlinea: multipla 1.3 ri

Formattato: Interlinea: multipla 1.3 ri



Afterwards, a parameter taken as comparison is computed in relation with the grade of refinement to understand the refinement beyond which is useless to go, since it will lead only to a higher computational cost while the result will not be affected. In this case the target parameter are the pressure drop due to the lamella, so computed between two planes 1 mm before and after the inlet and the outlet of the flow straightener and the axial velocity (average, maximum and minimum values) in two different planes, in the middle of the flow straightener and in the middle of the outlet pipe, as shown in FIGURE 20.

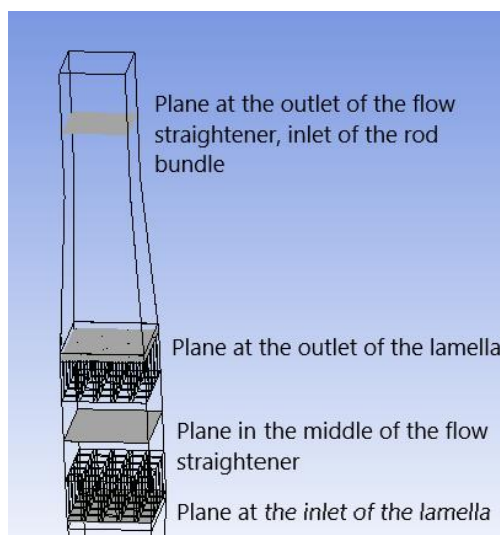


FIGURE 20: Location of the planes

These parameters are then computed in relation to the number of elements of the different meshes shown in [Table 3](#). The results are shown in [FIGURE 21](#), [FIGURE 22](#), [FIGURE 23](#), [FIGURE 24](#), [FIGURE 25](#) and [FIGURE 26](#).

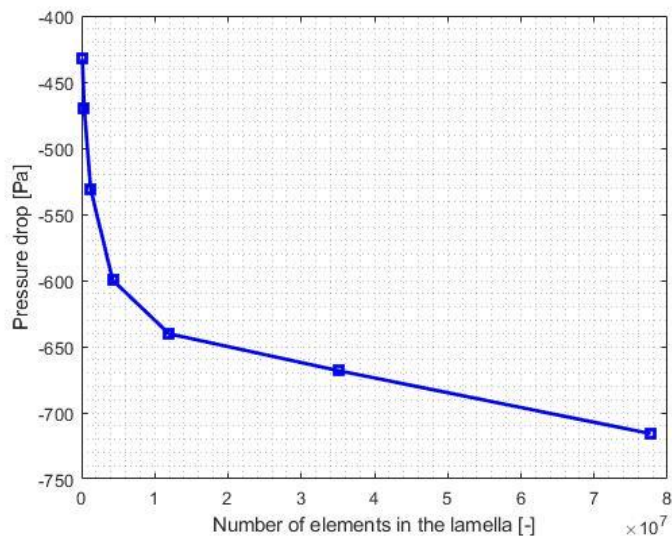


FIGURE 21: Pressure drop through the flow straightener - Number of elements

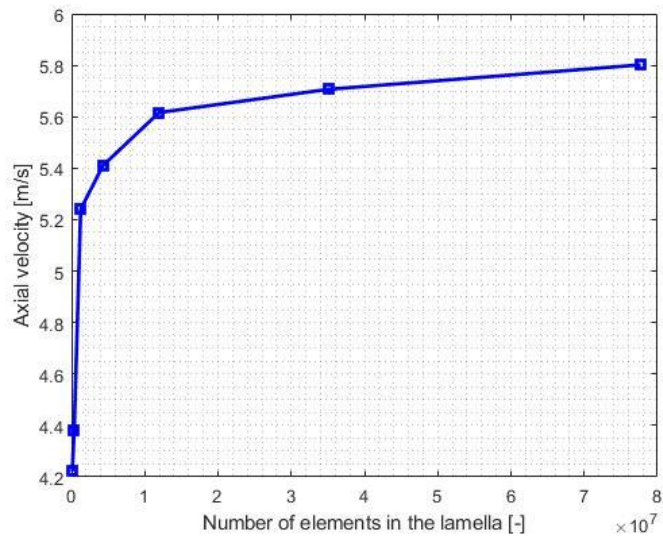


FIGURE 22: Maximum axial velocity in the middle plane - Number of elements

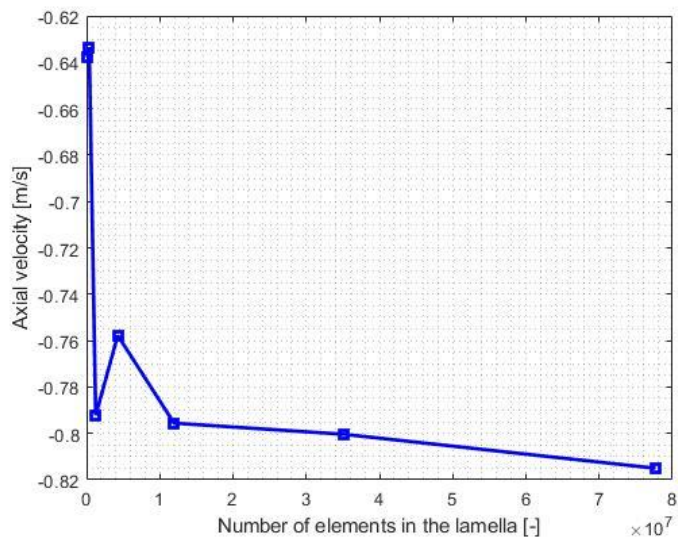


FIGURE 23: Minimum axial velocity in the middle plane - Number of elements

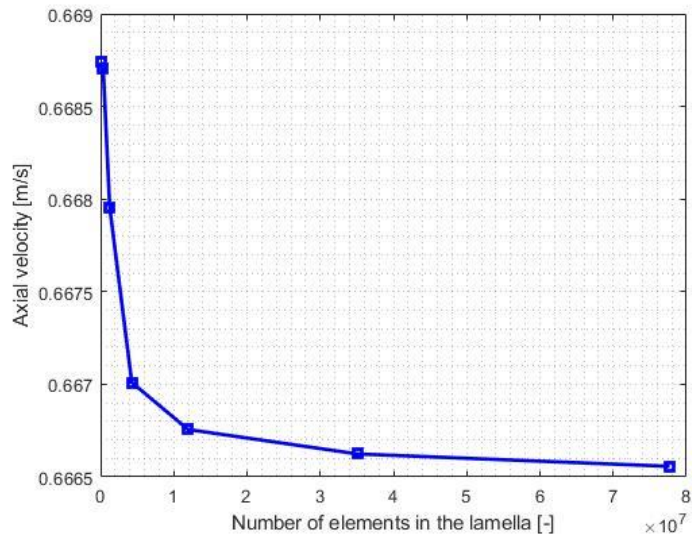


FIGURE 24: Average axial velocity in the middle plane - Number of elements

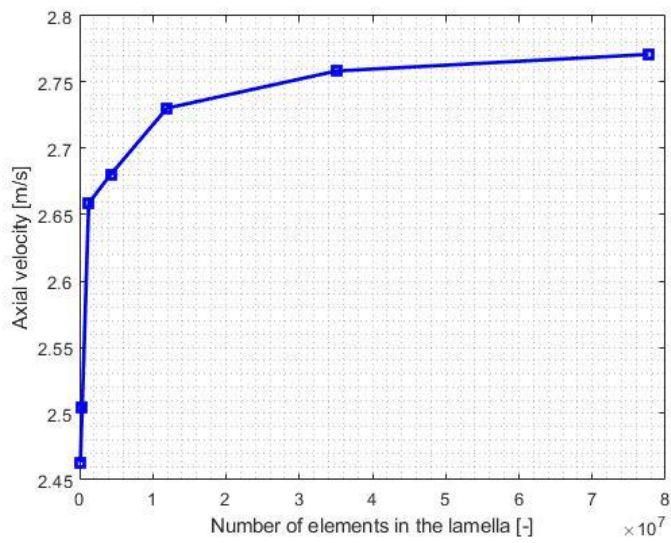


FIGURE 25: Maximum axial velocity in the outlet plane - Number of elements



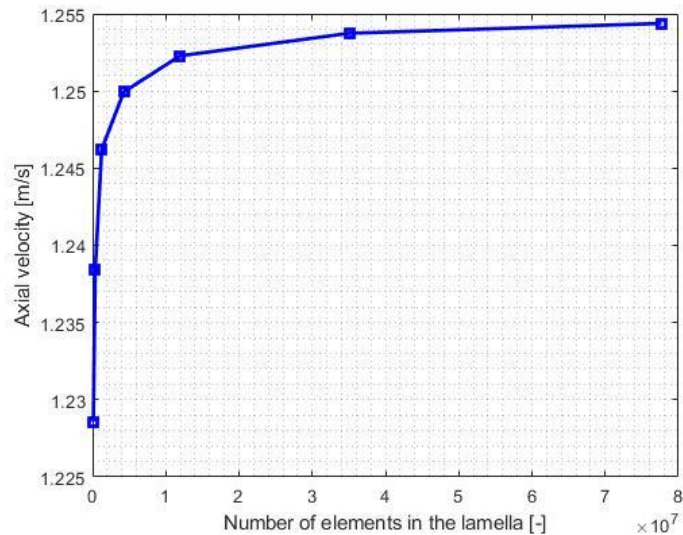


FIGURE 26: Average axial velocity in the outlet plane - Number of elements

Analyzing the results coming from the grid independence analysis, that show a good convergence especially at the outlet of the flow straightener, the M5 mesh was chosen to perform the turbulence analysis and to compare the results with the PIV experiments. The choice was made considering that this grid introduces an uncertainty, as it can be seen that in the previous plots the parameters are still going to convergence, but it is a tradeoff between the computational cost and the quality of the results.

### 5.3 PIV setup and experiments

To be able to perform PIV experiments on the area of interest, the PIV setup should be adapted at the geometry. In the case of the flow straightener, the investigation areas are the planes parallel to the streamwise direction, taking into account the flow inside different part of the grid. This is necessary due to the presence of the elbow: as can be seen in FIGURE 12, different channels of the flow straightener will see different velocities, since the central part of the flow straightener will have a higher velocity field, feeling more the elbow effect. For this reason, the PIV experiments were carried out over three different planes inside the flow straightener that are shown in FIGURE 27, where it can be seen that the plane 1 pass through the center of the middle channel of the grids,

while the 2 and 3 are investigating respectively planes far 10.4 mm and 20.8 mm from the central one, corresponding to the center of other two channels of the grids.

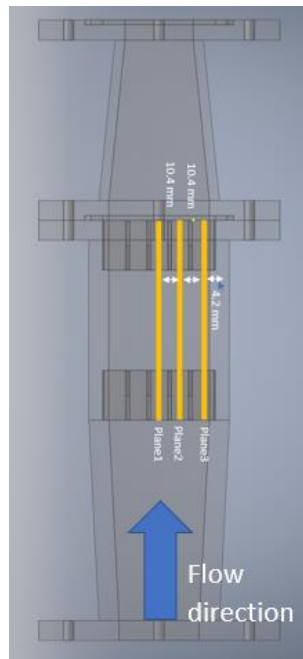


FIGURE 27: Monitoring plan of the PIV experiments

In order to obtain data about the axial velocity in these planes, the PIV setup had to be adapted to the geometry. Therefore, the laser was placed in front of the flow straightener so that the laser beam could hit perpendicularly the monitoring planes. The camera instead, referring to , was placed on the right side of the flow straightener, so that pictures could be taken of the plane hit by the laser. In FIGURE 28 a picture of the setup can be seen, and a schematic representation for a better understanding is shown in FIGURE 29, where a view from the top is adopted and also the planes are represented.

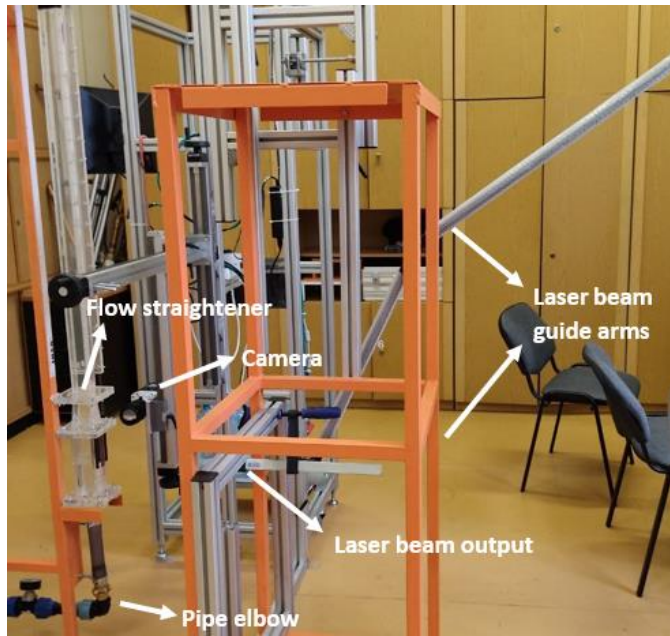


FIGURE 28: Picture of the PIV setup in BME laboratory

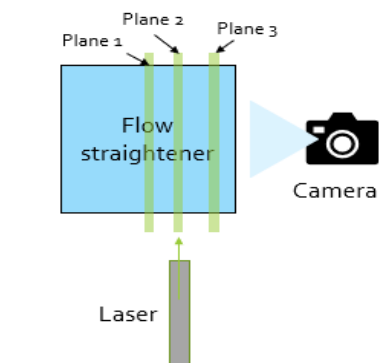


FIGURE 29: Schematic view of the PIV setup

The output of the PIV experiments, after some processing of the data by Dantec DynamicStudio, is the axial velocity field in the plane. An example about the result for plane 1 is shown in FIGURE 30.

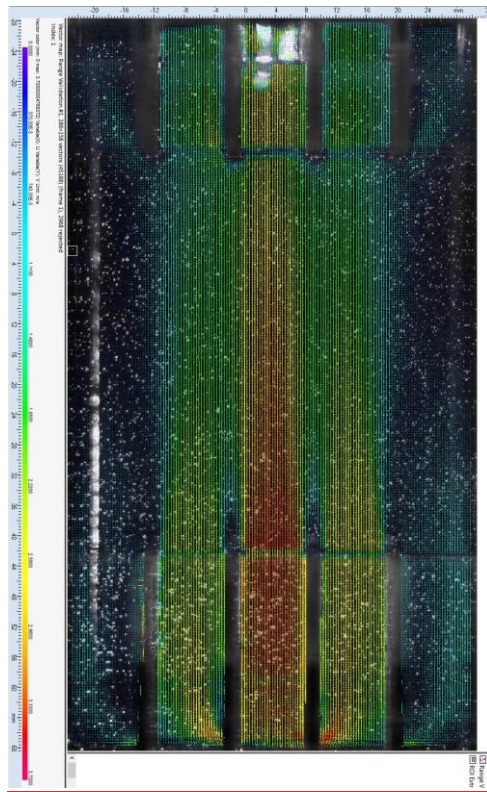


FIGURE 30: Axial velocity field for plane 1, PIV experiment output

It is clear that a comparison between such data and the one coming from the CFD simulations will be hard, since only a qualitative comparison based on the observation of the flow behavior will be possible. Such comparison will be hard and will not lead to a precise conclusion regarding the validation of the model. Therefore, it has been chosen to compare the axial velocity field picking some monitoring lines in each plane, so that the velocity profile could be compare. The positions of the monitoring lines can be seen in FIGURE 31, where they are drawn on the PIV output of the plane 1, in order to better understand where they are located, and in FIGURE 32, where more detailed geometry information are given. These monitoring lines allow to compare the axial velocity field along them between the PIV experiments and the CFD simulations. For simplicity they were drawn only in case of the plane 1, but the same solution is adopted for plane 2 and plane 3 too.

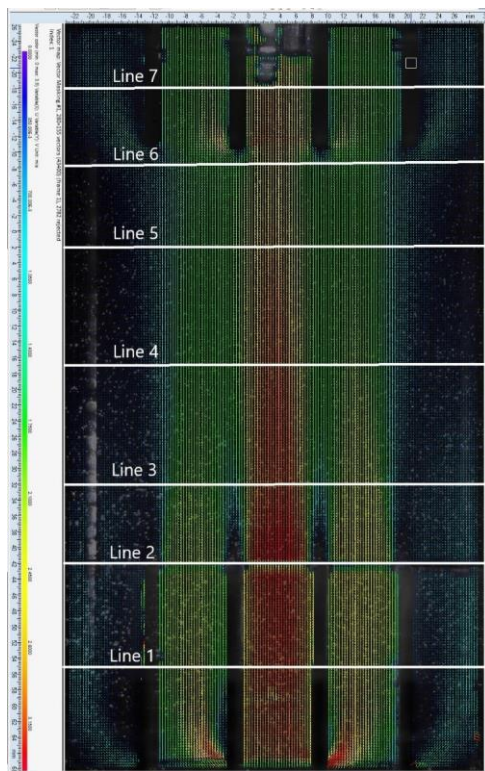


FIGURE 31: Monitoring lines

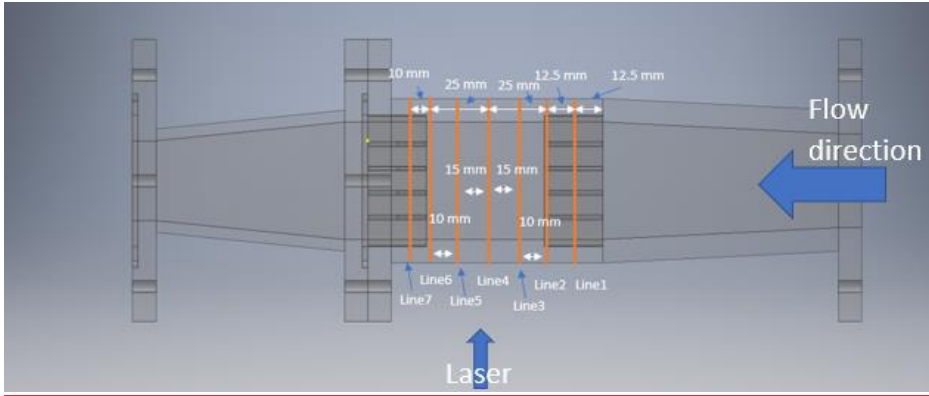


FIGURE 32: Geometry details about the monitoring lines

#### 5.4 Comparison of the results

In this section the axial velocity profiles along the lines shown in FIGURE 32 for each plane shown in FIGURE 27 are plotted for simulations using different turbulent models. They are then compared to the PIV experiments results to understand which model is better simulating the real behavior of the flow. The first turbulent model investigated is  $k-\epsilon$  that consists in two transport equations one for the turbulent kinetic energy  $k$  and a further one for the rate of dissipation of turbulent kinetic energy  $\epsilon$ . An evolution of the  $k-\epsilon$  model, the RNG (Re-Normalization Group)  $k-\epsilon$ , has been investigated: it consists in removing the small scales of motion from the governing equations by expressing their effects in terms of larger scale motions and a modified viscosity. It has been demonstrated that the  $k-\epsilon$  model doesn't offer a good description of the flow in the regions next to the wall. For this reason, the SST  $k-\omega$  model has been investigated too. It consists in a transformation from the  $k-\epsilon$  model into the  $k-\omega$  model into the near wall region (solving the equations in function of the turbulence kinetic energy and of the turbulence frequency), while the standard  $k-\epsilon$  model is adopted into the fully turbulent region. Basically, for what concerns the near wall region, the turbulence kinetic energy equation is the same solved by the standard  $k-\omega$  model, while the equation for the turbulence frequency arises from the equation of the  $k-\epsilon$  model for the rate of dissipation of turbulence kinetic energy substituting  $\epsilon = k \cdot \omega$  by definition. At the end, a more complicated model such as BSL Reynolds stress model has been used, that consist in the linear eddy viscosity assumption and the turbulence transport equations of the  $k-\omega$  SST, with additive terms accounting for the error due to the model-form.

The comparison between the PIV data and the turbulence models is reported from FIGURE 33 to FIGURE 39 for the plane 1. It can be seen that in the central part there is an overestimation of the value of the velocity, while in general the shape is quite the same for the all turbulence model and the PIV experiment. Outside the grids it can be seen that the overestimation is lower, and the shape is quite similar. In general, it can not be chosen a turbulence model that models better the behavior of the flow, since every model is closer to the PIV data in one region, but farer in another one.

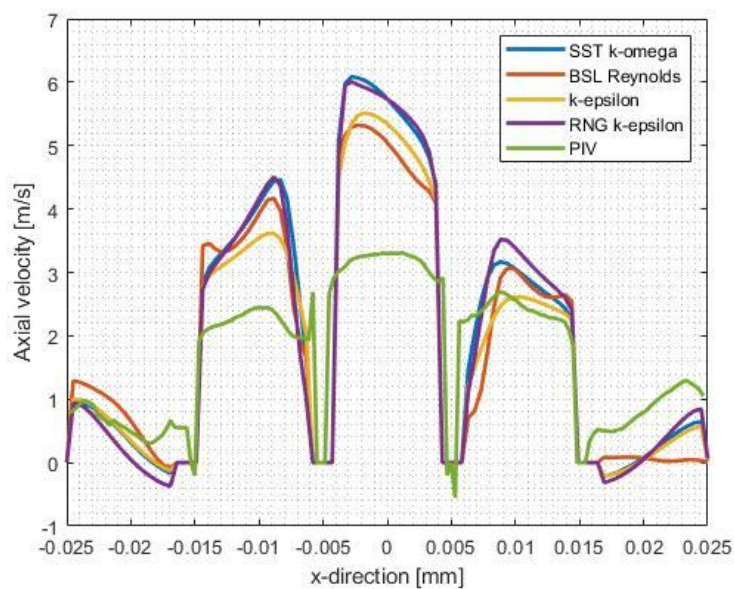
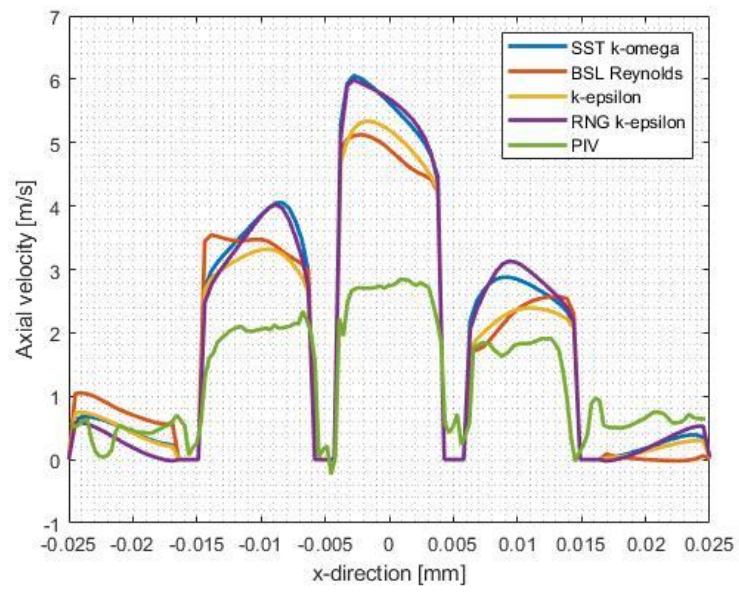


FIGURE 33: Axial velocity profile along Plane1 Line1

Codice campo modificato





*FIGURE 34: Axial velocity profile along Plane1 Line2*



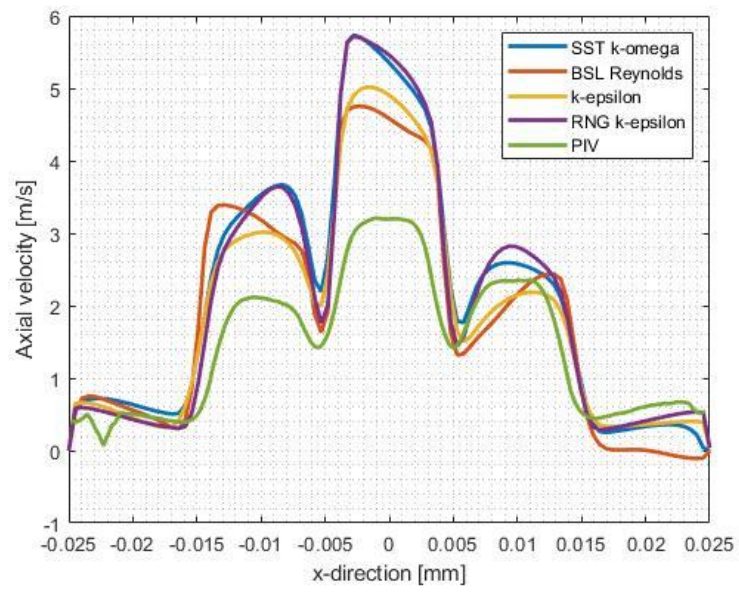


*FIGURE 35: Axial velocity profile along Plane1 Line3*

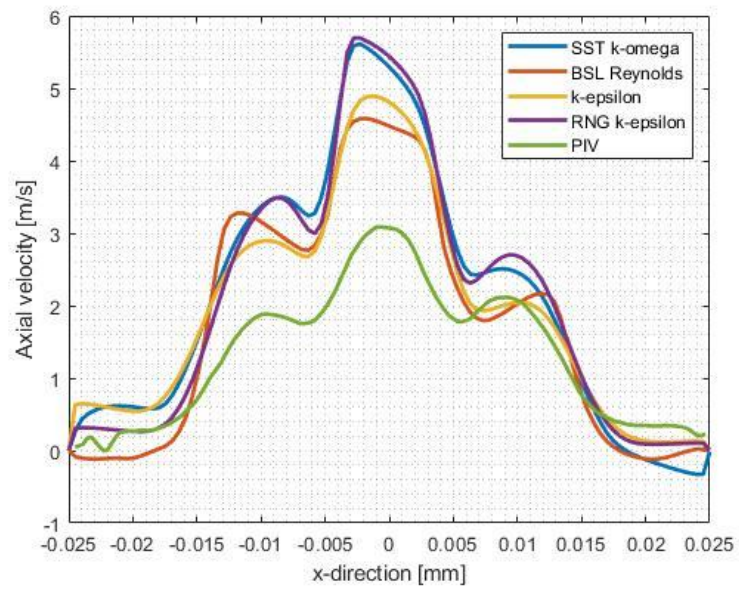


*FIGURE 36: Axial velocity profile along Plane1 Line4*

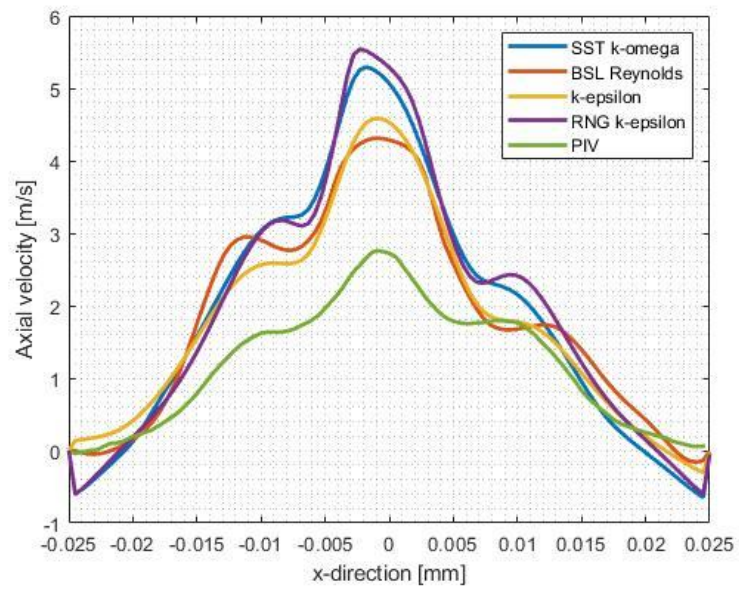
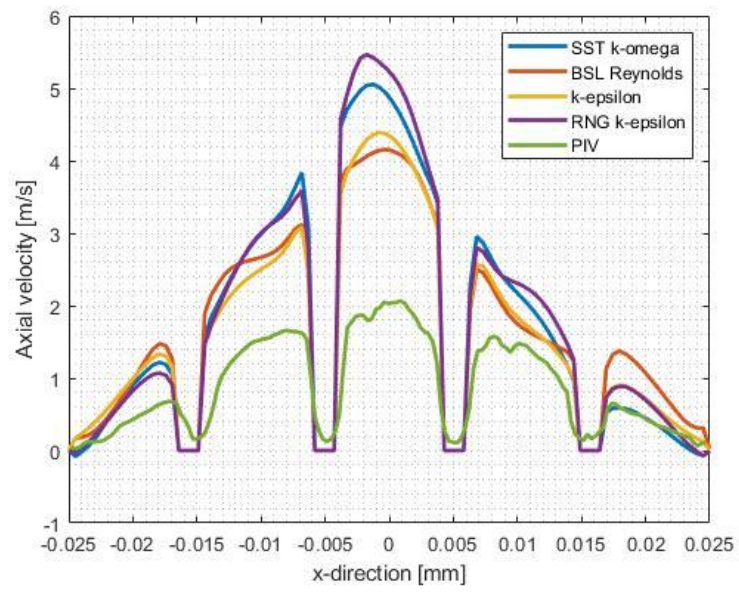


FIGURE 37: Axial velocity profile along Plane1 Line5



*FIGURE 38: Axial velocity profile along Plane1 Line6*

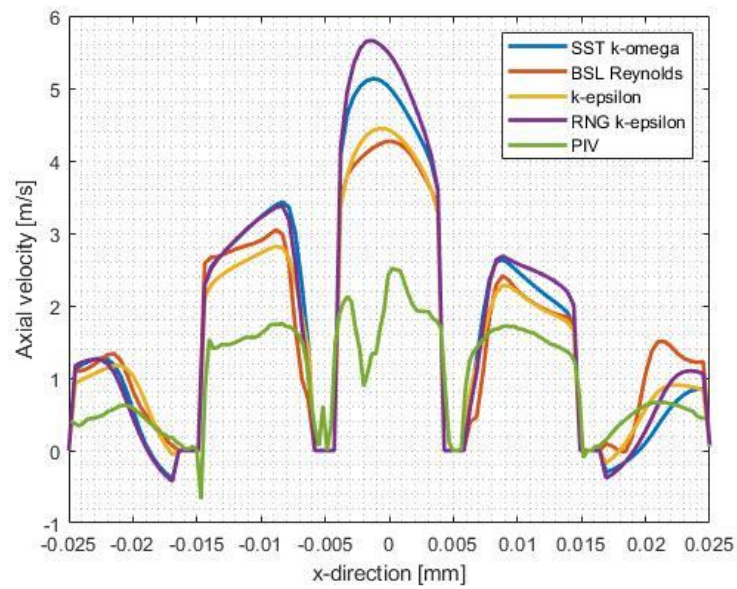
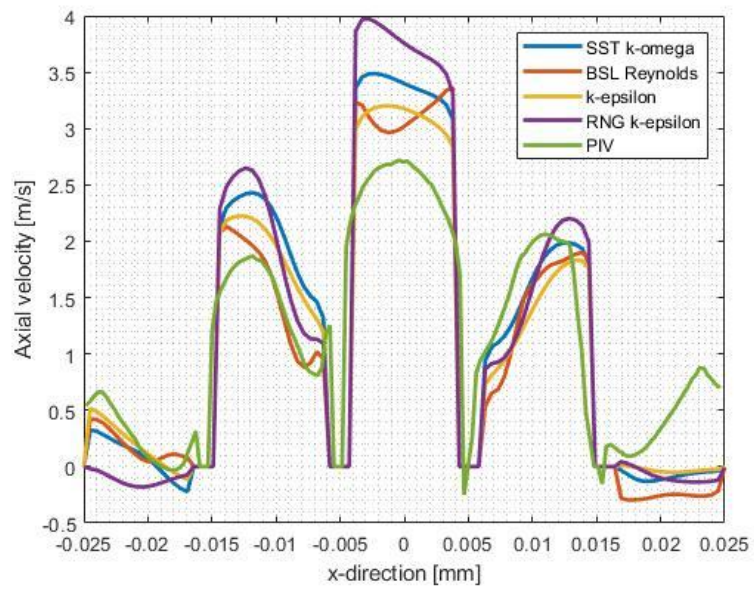
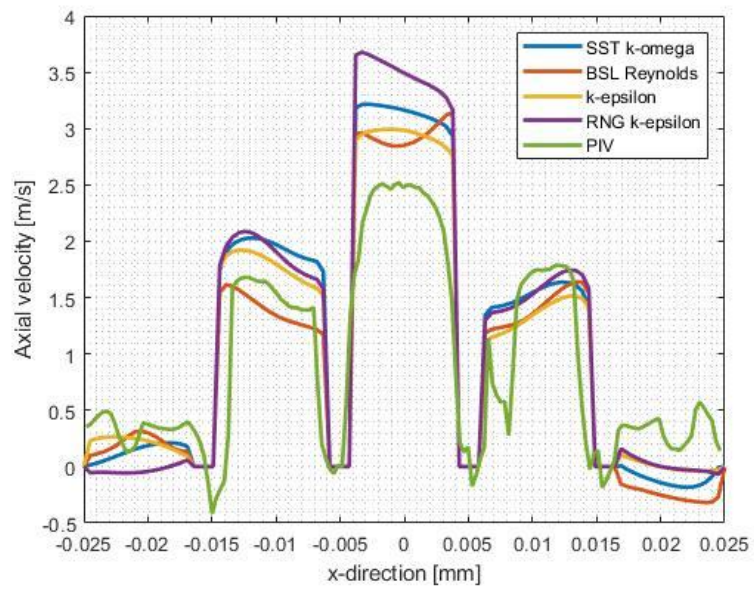


FIGURE 39: Axial velocity profile along Plane1 Line7

From FIGURE 40 to FIGURE 46 the comparison between the different turbulence model and the PIV data is reported in case of plane 2. A better correspondence between the two cases can be seen, especially for the k- $\epsilon$  model. The values of velocity are lower respect to the ones in plane 1. Near the wall, especially in the side channels of the lamellas, it seems that the turbulence models have more difficulties at simulating the behavior of the flow, and they underestimate the value of the velocity.



*FIGURE 40: Axial velocity profile along Plane2 Line1*



*FIGURE 41: Axial velocity profile along Plane2 Line2*



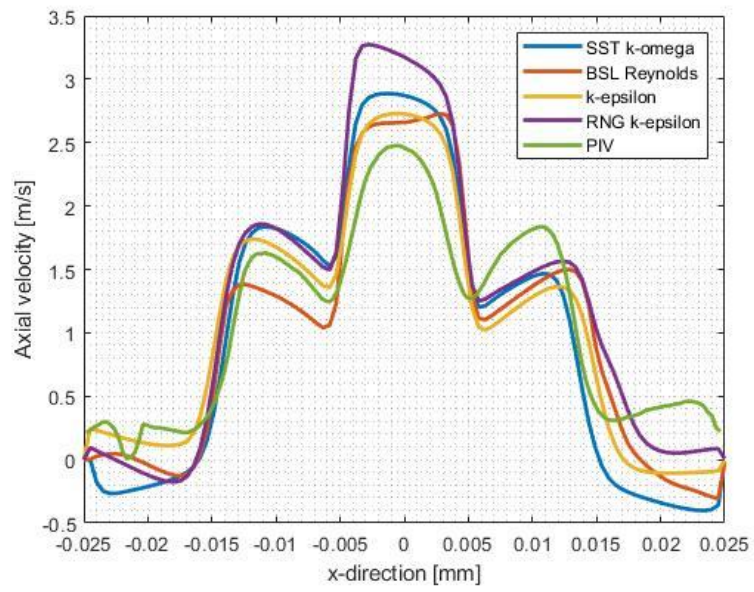


*FIGURE 42: Axial velocity profile along Plane2 Line3*



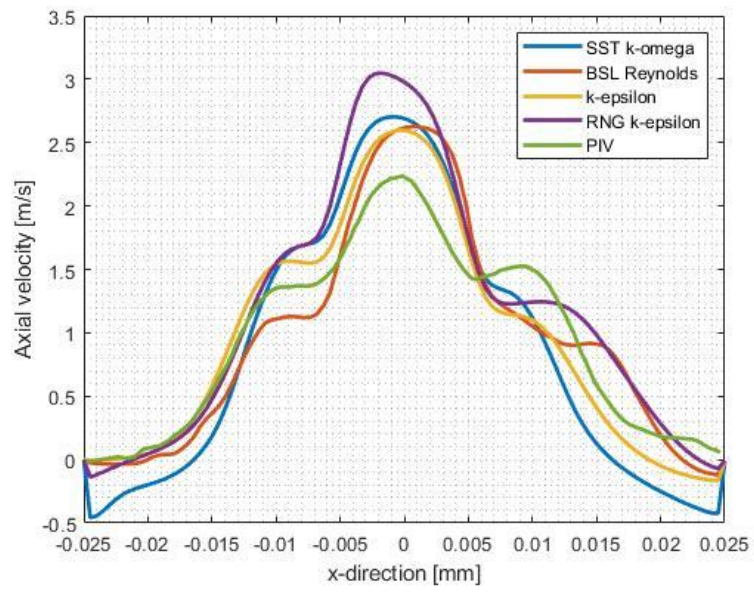


*FIGURE 43: Axial velocity profile along Plane2 Line4*

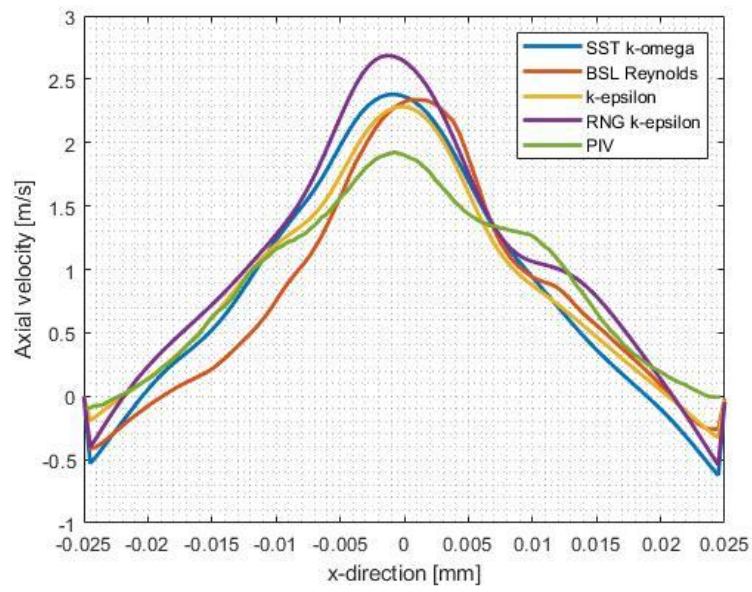


*FIGURE 44: Axial velocity profile along Plane2 Line5*

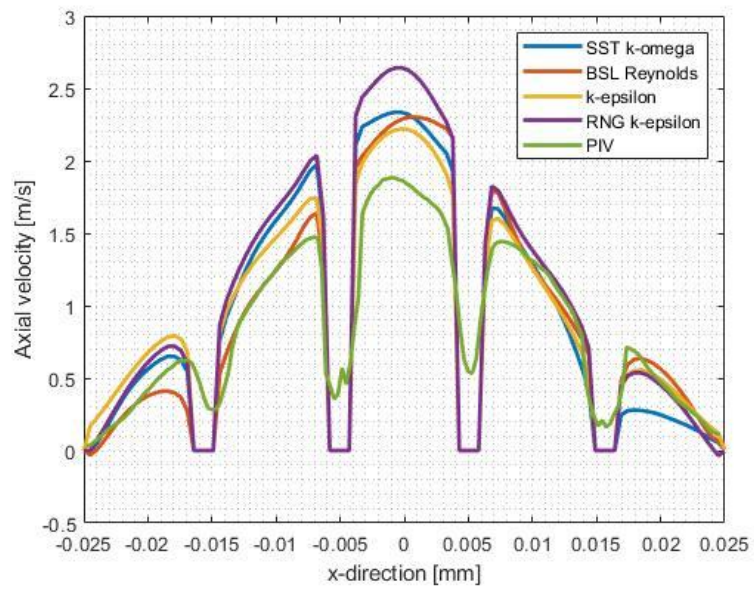


*FIGURE 45: Axial velocity profile along Plane2 Line6*

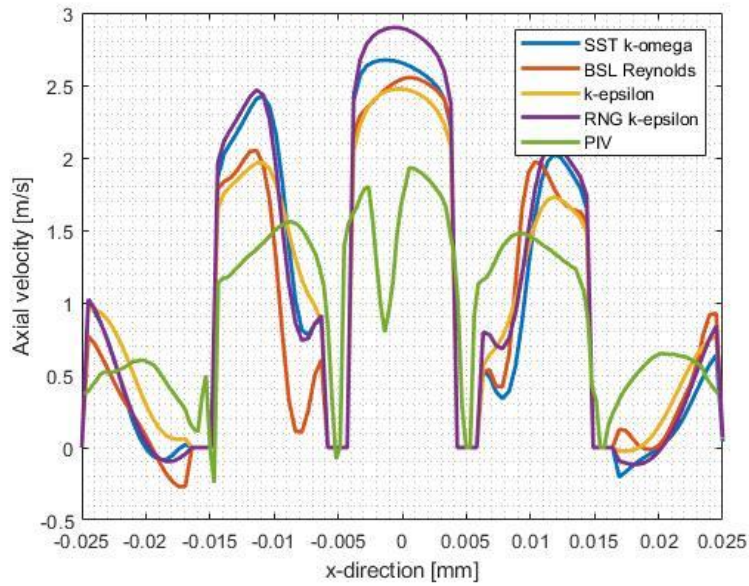


FIGURE 46: Axial velocity profile along Plane2 Line7

From FIGURE 47 to FIGURE 53 the comparison between the different turbulence model and the PIV data is reported in case of plane 3. It can be seen that in this case the correspondence between the simulations and the PIV data is harder, and even the velocity profile is not always the same. The model that manages better to simulate the behavior of the flow is still k- $\epsilon$  model, with the exception of the regions near the wall, where it's known that this model is not really precise. The values of the velocity are lower compared to the ones in plane 1 and plane 2, and in most of the cases a negative value of velocity, that it's symptom of counterflow, can be detected.

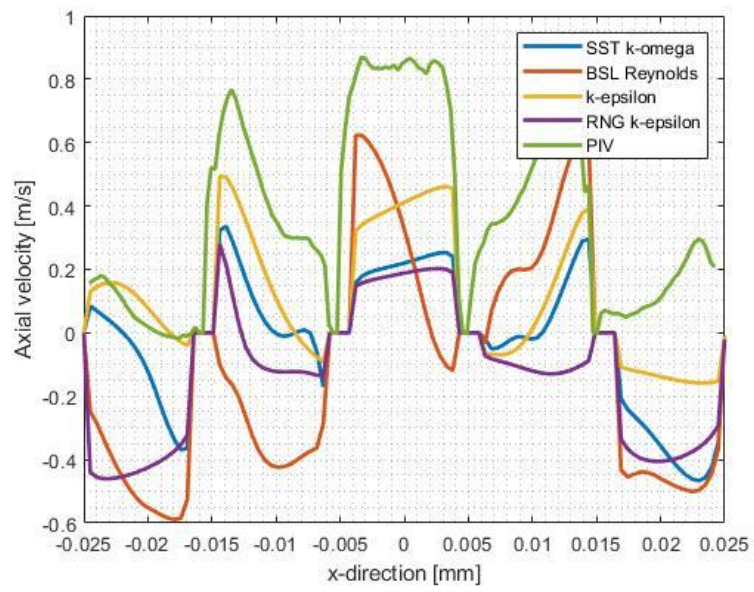
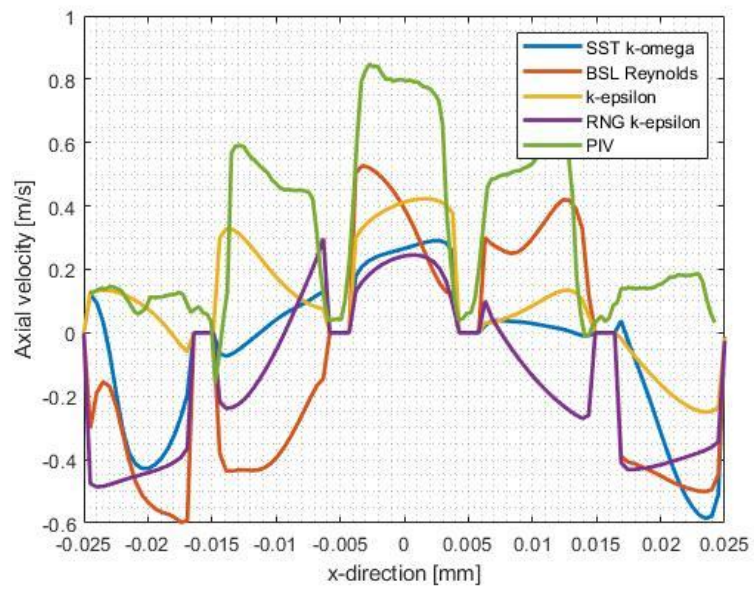


FIGURE 47: Axial velocity profile along Plane3 Line1



*FIGURE 48: Axial velocity profile along Plane3 Line2*

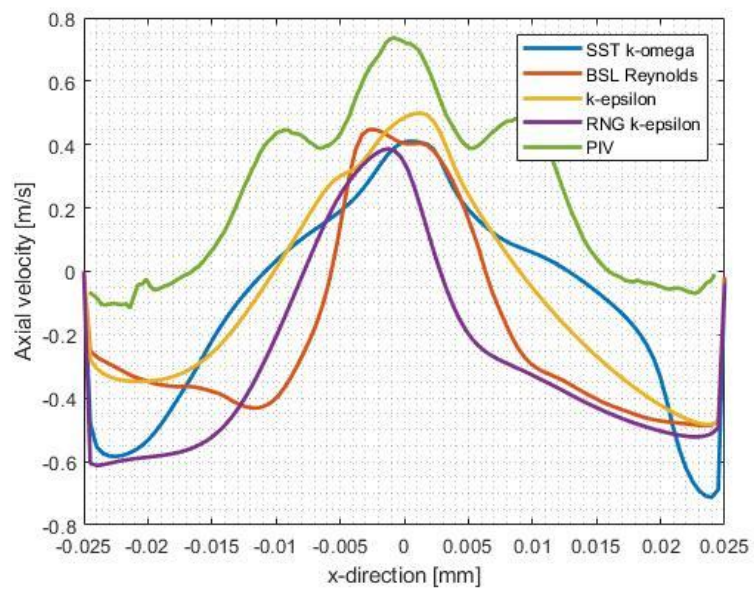
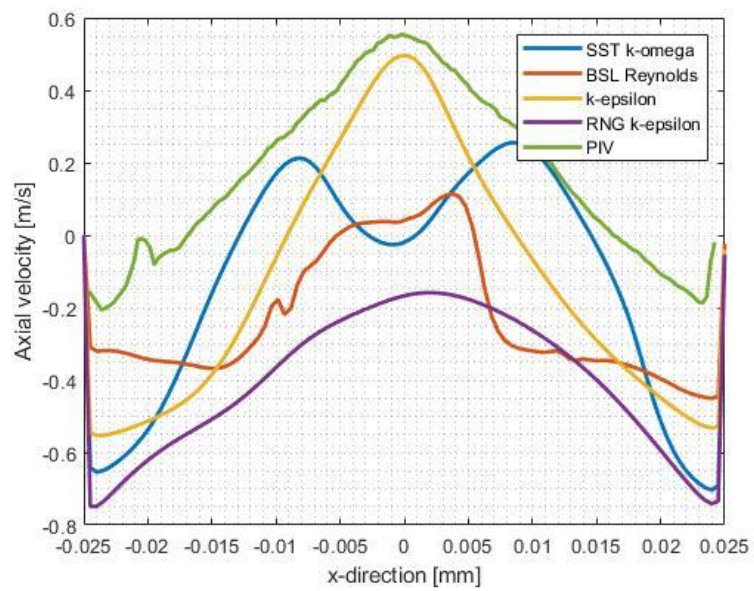


FIGURE 49: Axial velocity profile along Plane3 Line3





*FIGURE 50: Axial velocity profile along Plane3 Line4*



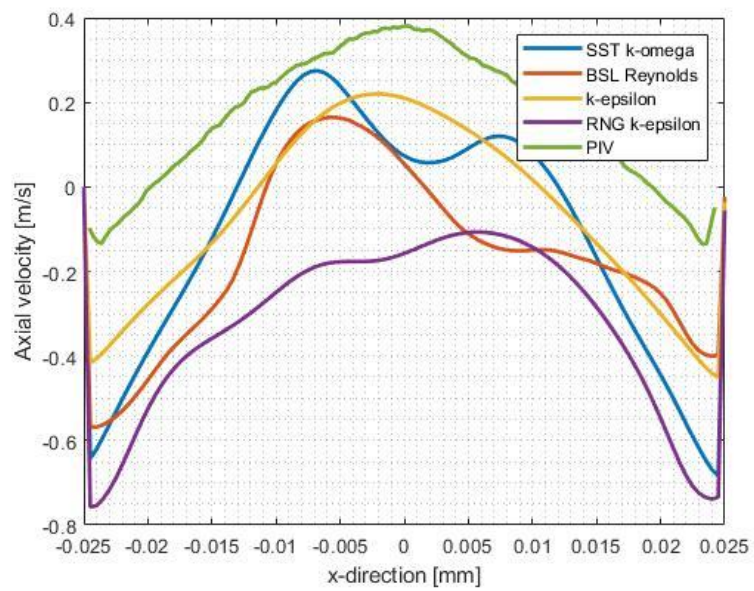


*FIGURE 51: Axial velocity profile along Plane3 Line5*

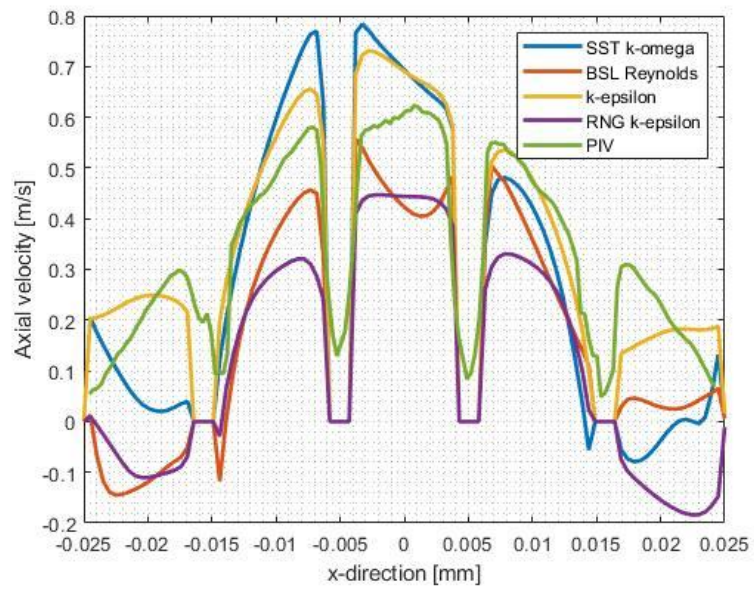


*FIGURE 52: Axial velocity profile along Plane3 Line6*

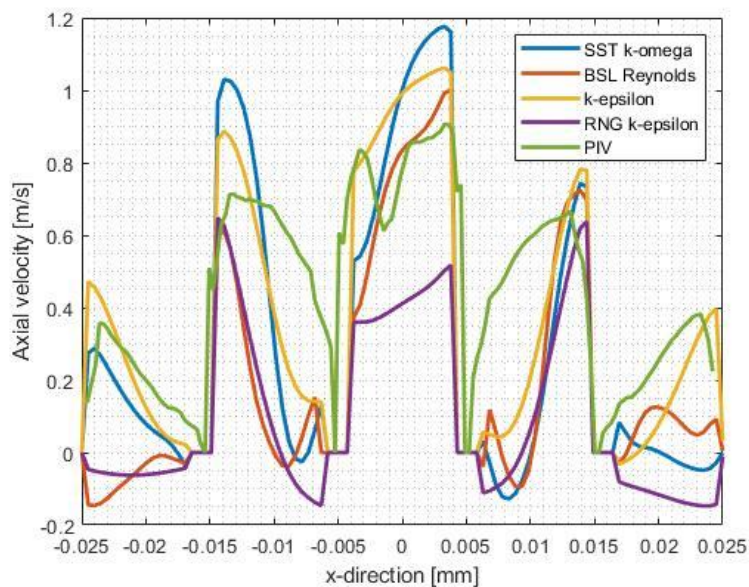


FIGURE 53: Axial velocity profile along Plane3 Line7

At the end of the turbulence analysis it seems clear that there is not a turbulence model that it's simulating better the real behavior of the flow. Since it's most of the cases there wasn't a compatibility between the simulations and the PIV data, this has lead to further investigations regarding the phenomenology of the flow.

#### 5.5 Phenomenology and unsteadiness of the flow

Doing the comparison between the PIV and the CFD data, it was seen an incompatibility of the results. In order to better understand what was happening from the hydraulic point of view, the axial velocity field was displayed in the planes showed in FIGURE 27, taking M5 as selected mesh. Starting from the inlet of the elbow, in FIGURE 54 it can be seen that the effect of the elbow is to accelerate the flow, especially in the outer part of it. After the elbow, due to the presence of a constriction, the velocity increases significantly, as shown in FIGURE 55. This makes the flow enters in the diffuser with a high velocity, like a jet, and due to the bigger area of the diffuser, a strong recirculation is present next to the wall and at the base of the diffuser as shown in FIGURE 56. In this same figure it's possible to see that the grids create three different peaks of velocity in the most central channel, while the velocity it's way lower in the channels next to the wall. The same behavior, with the creation of these three

Codice campo modificato

peaks in correspondence of the three most central channels, can be seen also in FIGURE 57 and in FIGURE 58, where the axial velocity field in the flow straightener is shown for plane 2 and plane 3. In these two latter figures it's possible to see the presence of a strong backflow. In plane 3 also the velocity field hasn't a clear pattern like in the plane 2, and the presence of some fluctuations of the velocity due to the presence of the grids can be detected.

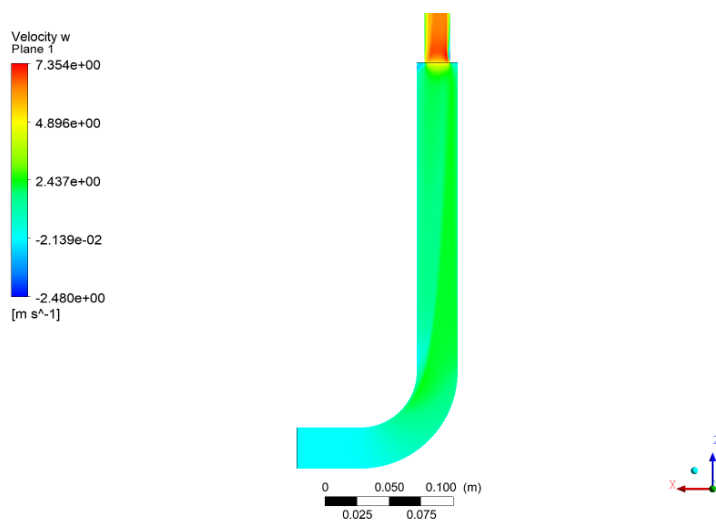
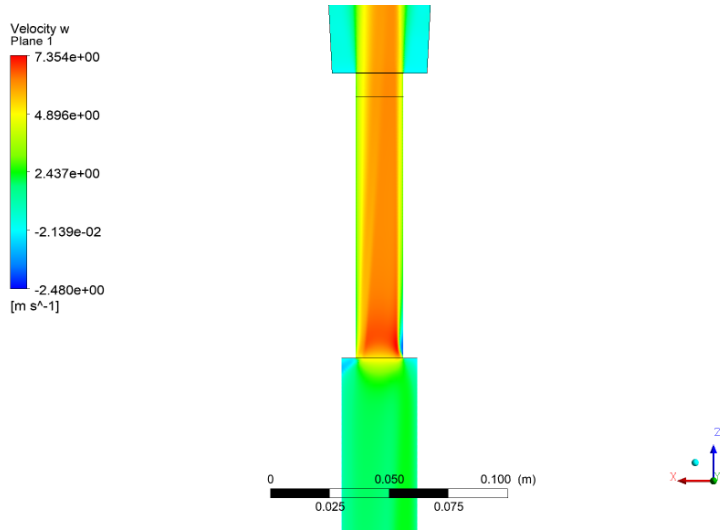
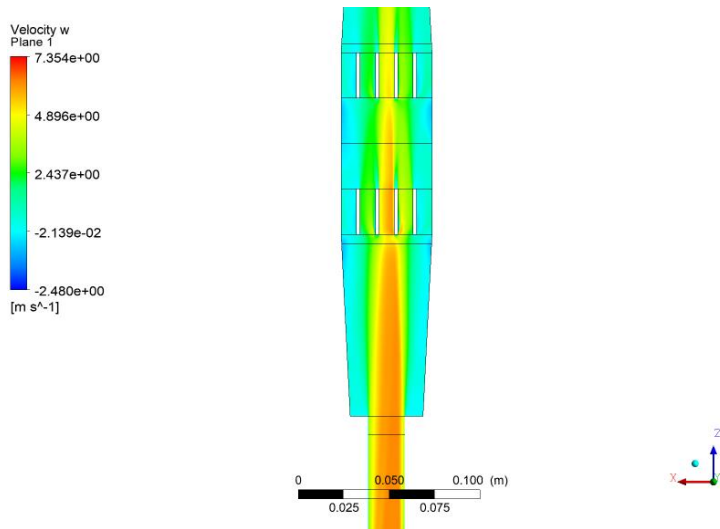


FIGURE 54: Axial velocity field in the elbow, plane 1



*FIGURE 55: Axial velocity field in the constriction, plane 1*



*FIGURE 56: Axial velocity field in the flow straightener, plane 1*

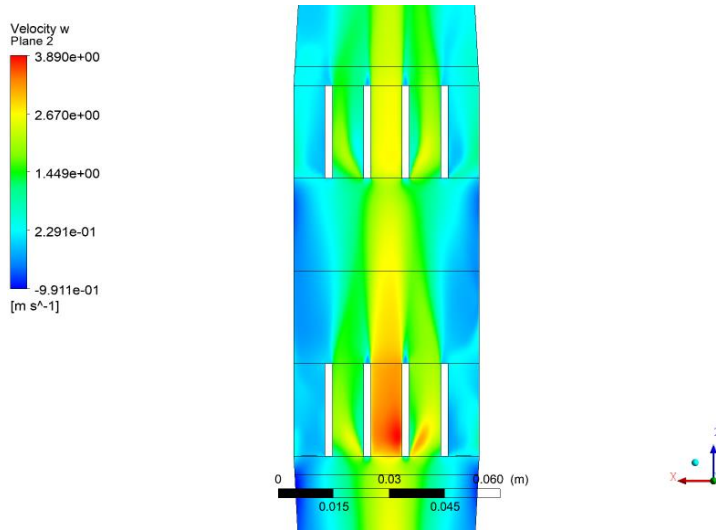


FIGURE 57: Axial velocity field in the flow straightener, plane 2

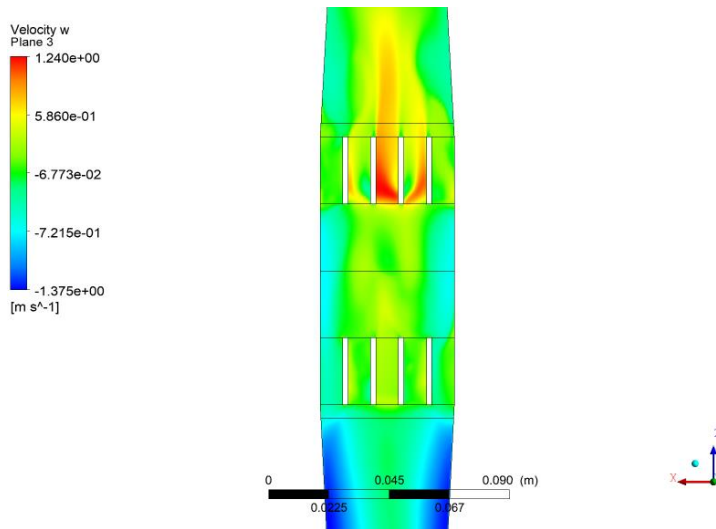


FIGURE 58: Axial velocity field in the flow straightener, plane 3

These latter evaluations are strictly qualitative, but it can be seen already that the flow has a particular behavior, related to the presence of the grids, that seems to hardly be steady state. In fact, the presence of the jet at the inlet of the flow straightener and the other ones created by the lamella makes the velocity field fickle. In order to have a confirm of this estimation, more quantitative

evaluations are needed. These can be performed for example comparing the profile of the velocity in different locations of the flow straightener: in FIGURE 59 the lines where the velocity profile is investigated are shown.

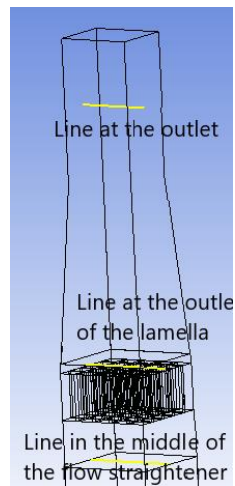


FIGURE 59: Lines for the comparison of the velocity profile

In FIGURE 60, FIGURE 61 and FIGURE 62 the velocity profiles along these lines can be seen.

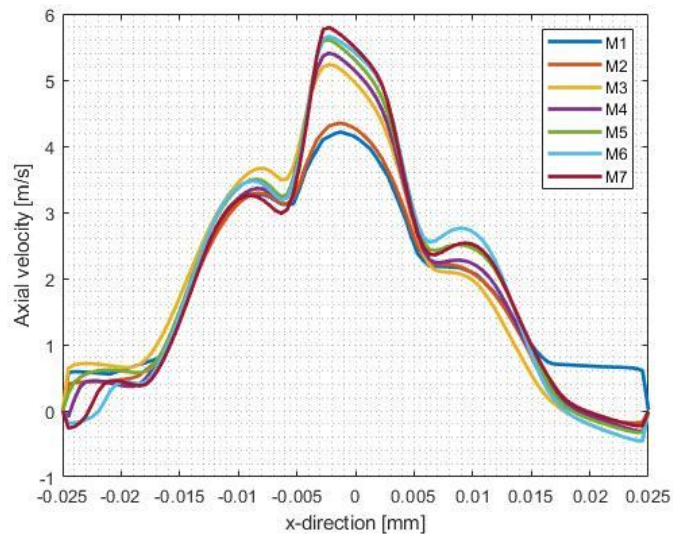


FIGURE 60: Axial velocity profile along a line in the center of the flow straightener

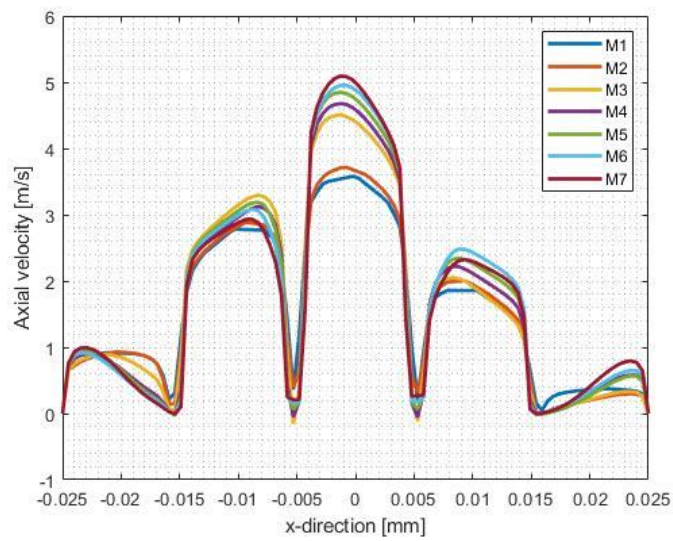


FIGURE 61: Axial velocity profile along a line at the outlet of the second grid



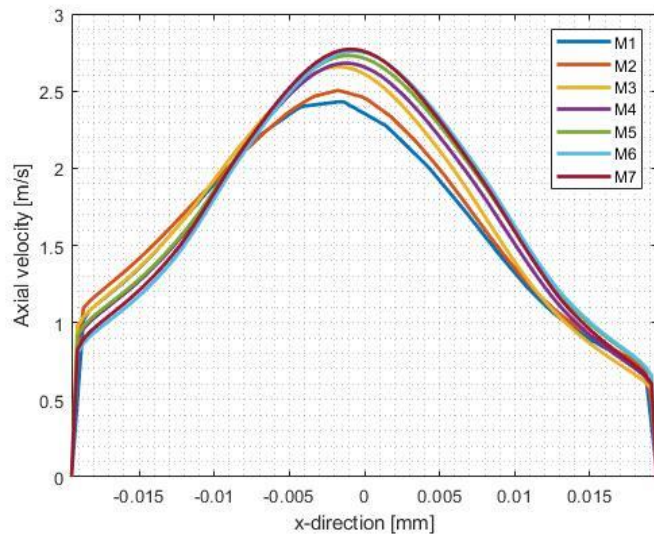


FIGURE 62: Axial velocity profile at the outlet of the flow straightener, inlet of the rod bundle

In these velocity profiles it can be seen that, in the case of the pic value, the velocity tends to go to a convergence value increasing the number of elements in the mesh. However, there are some locations where the values of a coarse and fine mesh are closer than the intermediate meshes, while in theory increasing the density of the mesh the value of the velocity should converge in every point of the domain. This doesn't totally confirm the sensation that the flow is unsteady, but it shows that there are some behaviors of the flow that need a better explanation.

To investigate this behavior, transient simulations were performed using Scale-Adaptive Simulation (SAS) model, that it's suitable for transient simulations. From these it was possible, thanks also to video materials that could be hardly shown in this contest, to understand that the presence of the elbow makes the flow unsteady, creating jets that make the value of the velocity fluctuate and making the convergence harder in all the parts. Some pictures of the axial velocity field in the transient simulation of M3 at different time instants are reported to better show this behavior. M3 was selected for this simulation since they are highly expensive both from the computational and the time point of view, and this mesh is a good trade-off between the resolution and the cost. In FIGURE 63, FIGURE 64 and FIGURE 65 the velocity is computed in plane 1. It can be seen the strong unsteadiness of the flow, with the peak of velocity moving from one side to another of the flow straightener and with the creations of many jets.

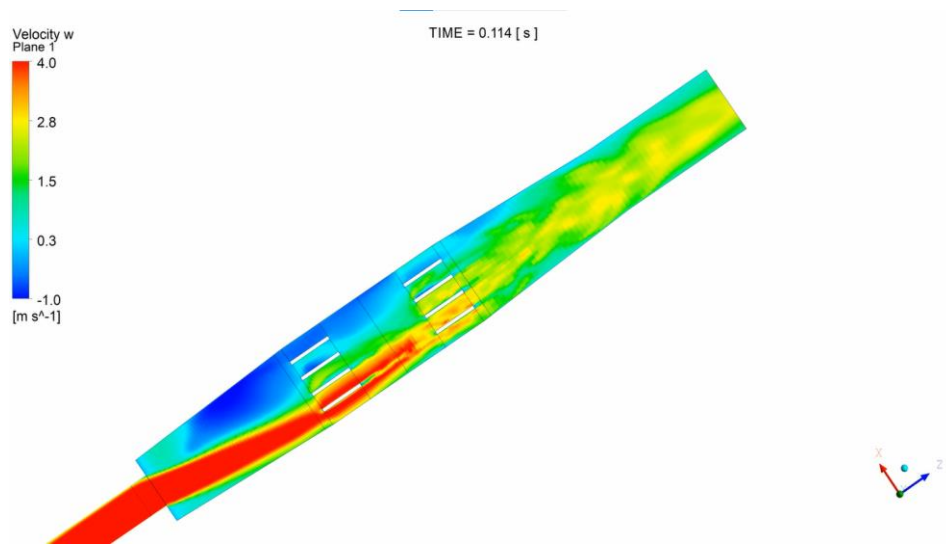


FIGURE 63: Axial velocity field at 0.114 s, plane 1

Codice campo modificato

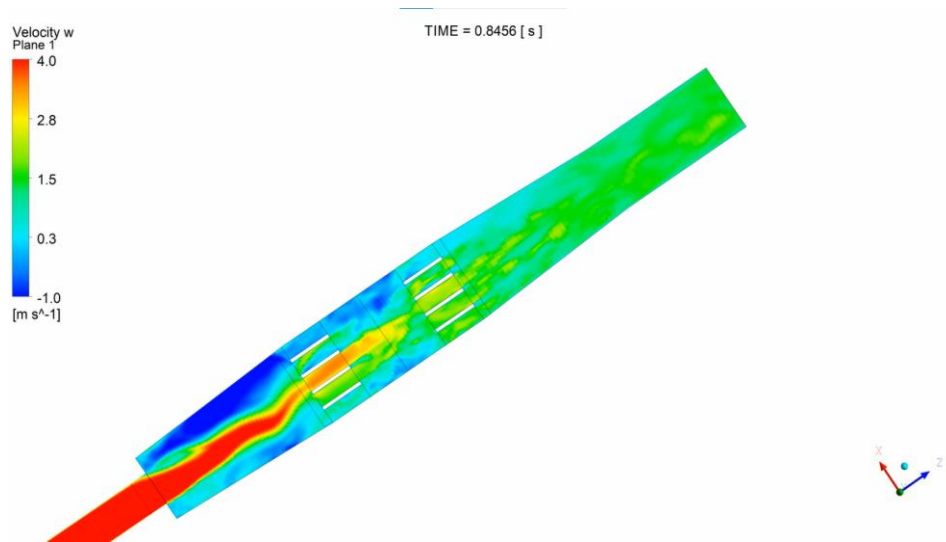


FIGURE 64: Axial velocity field at 0.8456 s, plane 1

Codice campo modificato

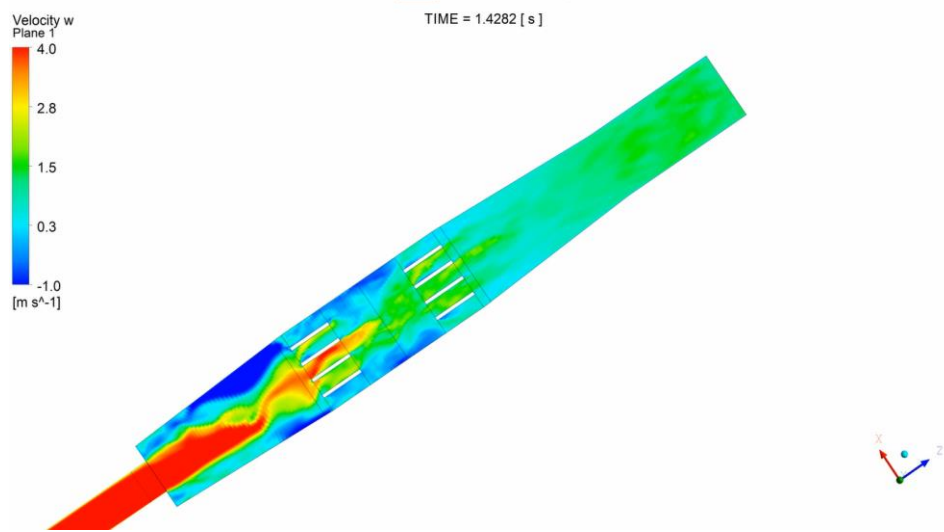


FIGURE 65: Axial velocity field at 1.4282 s, plane 1

It can be seen that the flow straightener is actually not doing the work for what it was installed at the start. The velocity profile at the outlet is way far to be uniform, but many jets are created. This is shown in FIGURE 66, FIGURE 67 and FIGURE 68.

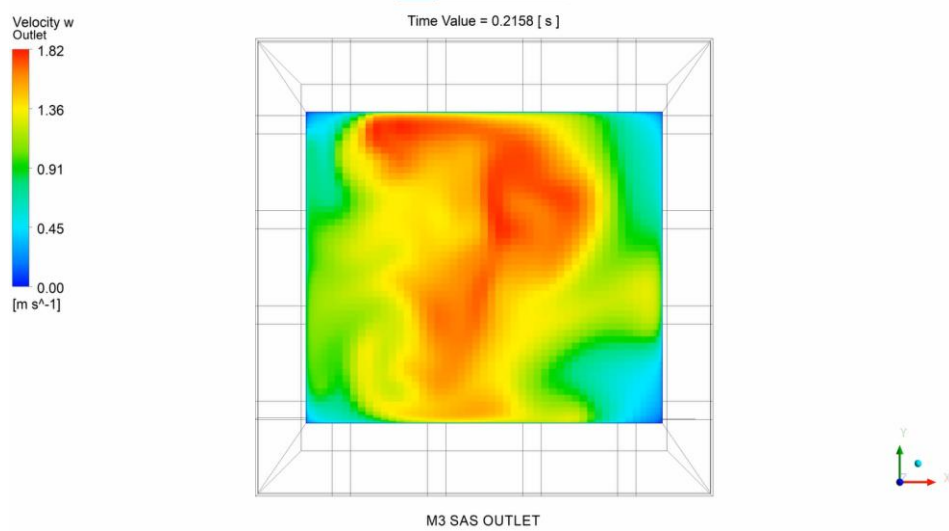
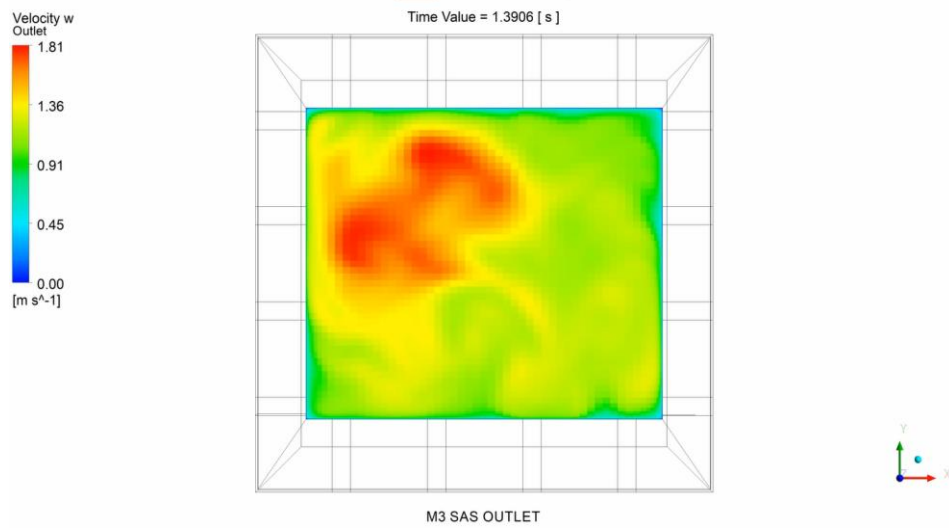


FIGURE 66: Axial velocity field at the outlet plane at 0.2158 s

Codice campo modificato

Codice campo modificato

Codice campo modificato



*FIGURE 67: Axial velocity field at the outlet at 1.3906 s*

Codice campo modificato

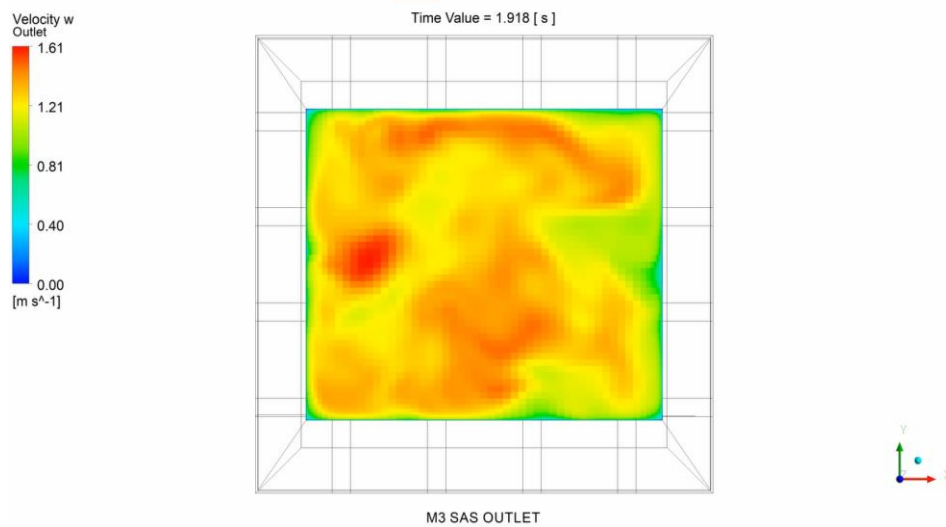


*FIGURE 68: Axial velocity field at the outlet at 1.918 s*

## 5.6 New designs

After this analysis it seems clear that the current design of the flow straightener is not compatible with the results that we would like to have. For this reason, new designs have been investigated. Due to a lack of time it will not be possible to show a full set of results, but only few suggestions of designs that could maybe help to design the new one. A full range of possibilities is available, but I've tried to start the new designs from the precious one, in order to understand if with some slightly modifications, saving money and time, it would be possible to have a better solution.

The first proposed design consists in keeping the flow straightener how it is, but change the end of the elbow part: It seems in fact that the restriction of the diameter at the outlet of the elbow causes an acceleration and an unsteady behavior of the flow, that then the flow straightener is not able to eliminate. This solution could be tricky due to that fact that it would be hard to change the hole present in the diffuser and to enlarge it due to presence of the joint between the two parts. In FIGURE 69 this design is shown.

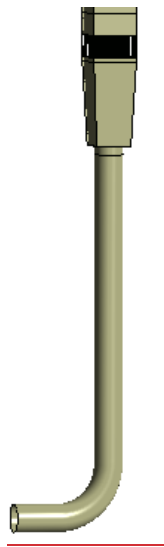


FIGURE 69: New design 1

Codice campo modificato

The second proposed design is to change the shape of the diffuser, reducing the area at the bottom of it, in order to have a more concentrated flow with less counterflow. This solution would require a change of the diffuser, but the diameter of the pipe could be the same and also the rest of the flow straightener. In FIGURE 70 this design is shown.

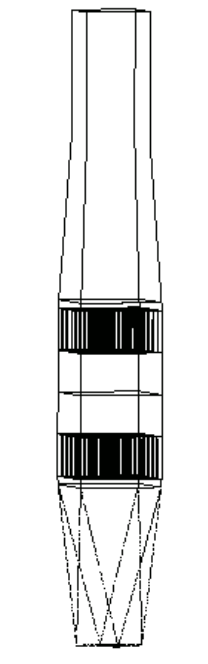


FIGURE 70: New design 2

The third and last design proposed in a new solution compared with the others. The shape of the flow straightener is completely changed: the confuser and the diffuser are eliminated, and the flow straightener has a constant quadratic section from the inlet to the outlet. The configuration of the grids is changed too: one is added at the end of the flow straightener with the same geometric characteristics then the first one, while the second one in the middle is designed in order to misalign the channels, avoiding the conditioning of the flow. In FIGURE 71 this design is shown.

Codice campo modificato



*FIGURE 71: New design 3*

In order to choose a new design a more accurate investigation would be needed, but to understand which one of these new suggested solutions allow to have a more uniform velocity field at the outlet point, i.e. the inlet point of the 7x7 section, the velocity profile along a line at the outlet is compared in FIGURE 72.

Codice campo modificato

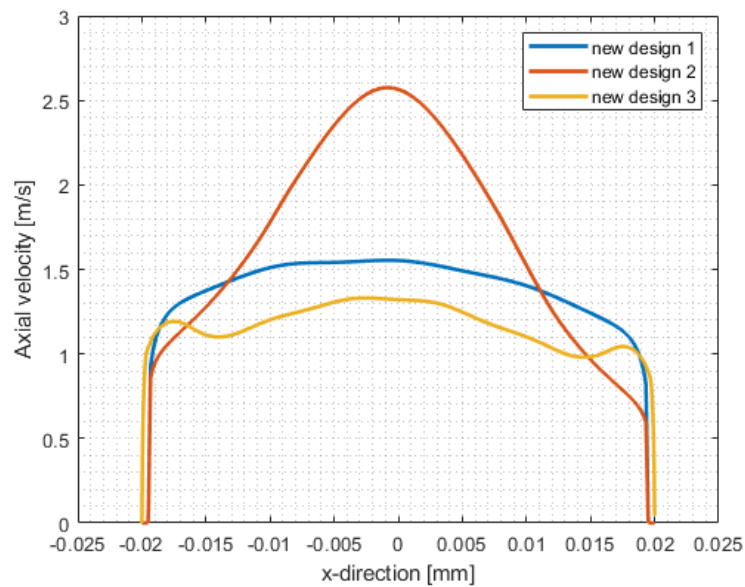


FIGURE 72: Velocity profile along the line at the outlet for different new designs

It can be seen that for the second design there is still a peak in the middle of the profile, while this doesn't happen in case of the design 1 and 3. In both cases the velocity profile is quite uniform, but it seems that the design 3 feels the conditioning coming from the constant section and the presence of the aligned lamellas. On the other hand, the design 1 shows a regular profile with a small increase of the velocity in the center.

It would be hard to determine which of these designs is the most suitable for reaching a better inlet condition of the test section only based on these results, but it seems that the restriction of diameter at the inlet of the flow straightener could be the responsible of the unsteadiness of the flow. Deeper investigations are needed, and it could be useful to perform also transient simulations on the chosen design, in order not to have again an unsteady flow.



## 1.6. Summary and conclusion

This thesis has been focused on the development of a CFD model and its validation through PIV measurements of the flow straightener placed at the entrance of the core of the ALLEGRO reactor.

At the development of the design of ALLEGRO also participates the Budapest University of Technology and Economics, where, in the faculty of natural science, a test loop for the hydraulics study of 7 pin ALLEGRO rod bundle has been build and is currently under investigation. In this loop, the installation of a flow straightener has been necessary in order to eliminate the conditioning coming from the elbow and to balance the inlet conditions of the test section giving a more homogeneous velocity field. My work was focused on the developing of a CFD model using (ICEM CFD 19.2 and CFX 19.2) that could simulate the behavior of the fluid in the flow straightener, validating then it by means of the PIV experiments. In particular, the velocity profile of the CFD model and the real one obtained through the PIV experiments have been compared on seven lines perpendicular to the flow for three different planes placed in different channels of the flow straightener, in steady state condition. This comparison hasn't led to the wanted results, since a considerable difference on the results was present. The analysis has been performed considering also different turbulence model with different grade of accuracy, but also in this case the quality of the results haven't changed. With a deeper and more sophisticated analysis, taking into account the time dependence, it came to notice that what was expected to be and was treated as a steady state flow, was in reality a fluctuant flow. These fluctuations were due to a reduction in the diameter of the pipe at the inlet of the diffuser of the flow straightener, causing an acceleration of the flow and the creation of jets. Since the goal of the flow straightener would have been to make the flow more stable, in this case the result was completely the opposite.

On the last part of my work, I have tried to develop a new realizable design for the flow straightener that would respect its goal. In particular the focus was on a design that would make the velocity profile as homogeneous as possible at the outlet of the flow straightener. The one respecting with this characteristic was a design where the reduction of the diameter was eliminated. Due to a lack of time, it was impossible to proceed on the investigation and realize the new flow straightener, but that would be the main focus for the next period. The new design of the flow straightener will be investigated and built in the future.

## References

- [1] IEA, "Key World Energy Statistics 2020," IEA, Paris, 2020.
- [2] IEA, "Nuclear Power in a Clean Energy System," IEA, Paris, 2019.
- [3] O. N. E. A. f. t. G. I. I. Forum, "Technology Roadmap Update for Generation IV Nuclear Energy Systems," 2014.
- [4] S. Tóth, A. Aszódi and G. I. Orosz, "Simulations for L-STAR experimental gas-cooled system," *Kerntechnik*, no. 5, p. 326–335, 2020.
- [5] C. F. McDonald, "The Key Role of Heat Exchangers in Advanced Gas-Cooled Reactor Plants," *Heat Recovery Systems and CHP*, no. 1, p. 7–28, 1994.
- [6] Y. Dong, "Design, Safety Features & Progress of HTR-PM," in *Generation IV International Forum [Online Conference]*, INET, Tsinghua University, China, January 24, 2018.
- [7] R. Zajac, B. Hatala and P. Darilek, "Overview of ALLEGRO project," in *Proceedings 21 International Conference on Applied Physics of Condensed Matter and of the Scientific Conference Advanced Fast Reactors*, Slovakia, 2015.
- [8] C. Poette, F. Morin, V. Brun-Magaud and J. Pignatel, "ALLEGRO 75 MW Cores Definition at Start of GOfASTR. (GoFastRDEL-1.2-01)," 2010.
- [9] S. Tóth, B. Kiss, E. Gyuricza and A. Aszódi, "CFD Investigation of ALLEGRO Fuel Assemblies," in *The 15th International Topical Meeting on Nuclear Reactor Thermal - Hydraulics, NURETH-15*, Pisa, Italy, May 12-17, 2013.
- [10] J. Kubačka, J. Remiš, R. G. de Leija, S. Scherrer and R. Kruessmann, "CFD Model of L-STAR/SL Loop-GoFastR Project," *4th International Youth Conference on Energy (IYCE)*, pp. 1-7, 2013.
- [11] M. Berthouex and T. Cadiou, "The thermal hydraulics in a rod bundle representative of the start-up core of the ALLEGRO Gas cooled Fast Reactor-Experimental and numerical approaches," *Nuclear Engineering and Design*, no. 10, pp. 3372-3386, 2010.
- [12] L. Bělovský, J. Gadò, B. Hatala, A. Vasile and G. Wrochna, "The ALLEGRO Experimental Gas Cooled Fast Reactor Project," in *International Conference on Fast Reactor and Related Fuel Cycles, Next Generation Nuclear Systems for Sustainable Development*, Yekaterinburg, Russia, June 26-29, 2017.

Codice campo modificato

**ha formattato:** Tipo di carattere: (Predefinito) +Corpo (Calibri), 11 pt, Colore carattere: Automatico

- [13] E. E. Dominguez-Ontiveros and Y. A. Hassan, "Non-intrusive experimental investigation of flow behavior inside a 5x5 rod bundle with spacer grids using PIV and MIR," *Nuclear Engineering and Design*, no. 5, pp. 888-898, 2009.
- [14] S. Jun, "The Progress of HTR-PM in China," in *Small and Advanced Reactors [Online Conference]*, Institute of Nuclear and New Energy Technology, Tsinghua University, Beijing, China, February 18, 2021.
- [15] W. J. Kim, D. Kim and J. Y. Park, "Fabrication and Material Issues for the Application of SiC Composites to LWR Fuel Cladding," *Nuclear Engineering and Technology*, no. 4, pp. 565-572, 2013.
- [16] Y. Lee, T. J. McKrell and M. S. Kazimi, "Thermal shock fracture of hot silicon carbide immersed in water," *Journal of Nuclear Materials*, p. 172-180, 2015.
- [17] A. Papukchiev and S. Buchholz, "Validation of ANSYS CFX for gas and liquid metal flows with conjugate heat transfer within the European project THINS," *Nuclear Engineering and Design*, p. 338-350, 2017.
- [18] P. Qi, P. Wang, S. Hao, K. Cheng, S. Qiao and S. Tan, "Experimental study of flow structures in a large range downstream the spacer grid in a 5 x 5 rod bundle using TR-PIV," *International Journal of Heat and Fluid Flow*, 108619, 2020.
- [19] W. Qu, J. Xiong, S. Chen and X. Cheng, "High-fidelity PIV measurement of cross flow in 5x5 rod bundle with mixing vane grids," *Nuclear Engineering and Design*, pp. 131-143, 2019.
- [20] Z. Zhang, Y. Dong, F. Li, Z. Zhang, H. Wang, X. Huang, H. Li, B. Liu, X. Wu, H. Wang, X. Diao, H. Zhang and J. Wang, "The Shandong Shidao Bay 200 MWe High-Temperature Gas-Cooled Reactor Pebble-Bed Module (HTR-PM) Demonstration Power Plant: An Engineering and Technological Innovation," *Engineering*, no. 1, pp. 112-118, 2016.

[1] IEA, "Key World Energy Statistics 2020," IEA, Paris, 2020.

[2] IEA, "Nuclear Power in a Clean Energy System," IEA, Paris, 2019.

[3] O. N. E. A. f. t. G. I. I. Forum, "Technology Roadmap Update for Generation IV Nuclear Energy Systems," 2014.

Formattato: Interlinea: multipla 1.3 ri

ha formattato: Inglese (Stati Uniti)

Formattato: Interlinea: multipla 1.3 ri

Formattato: Interlinea: multipla 1.3 ri

- [4] S. Tóth, A. Aszódi and G. I. Orosz, "Simulations for L-STAR experimental gas-cooled system," *Kerntechnik*, no. 5, p. 326–335, 2020.
- [5] C. F. McDonald, "The Key Role of Heat Exchangers in Advanced Gas-Cooled Reactor Plants," *Heat Recovery Systems and CHP*, no. 1, p. 7–28, 1994.
- [6] Y. Dong, "Design, Safety Features & Progress of HTR-PM," in *Generation IV International Forum [Online Conference]*, INET, Tsinghua University, China, January 24, 2018.
- [7] R. Zajac, B. Hatala and P. Darilek, "Overview of ALLEGRO project," in *Proceedings 21<sup>st</sup> International Conference on Applied Physics of Condensed Matter and of the Scientific Conference Advanced Fast Reactors*, Slovakia, 2015.
- [8] C. Poette, F. Morin, V. Brun-Magaud and J. Pignatelli, "ALLEGRO 75 MW Cores Definition at Start of GOFSTR. (GoFastRDEL 1.2-01)," 2010.
- [9] S. Tóth, B. Kiss, E. Gyuricza and A. Aszódi, "CFD Investigation of ALLEGRO Fuel Assemblies," in *The 15th International Topical Meeting on Nuclear Reactor Thermal-Hydraulics, NURETH-15*, Pisa, Italy, May 12–17, 2013.
- [10] J. Kubačka, J. Remiš, R. G. de Leija, S. Scherrer and R. Kruessmann, "CFD Model of L-STAR/SL Loop GoFastR Project," *4th International Youth Conference on Energy (IYCE)*, pp. 1–7, 2013.
- [11] M. Berthouex and T. Cadiou, "The thermal hydraulics in a rod bundle representative of the start-up core of the ALLEGRO Gas-cooled Fast Reactor: Experimental and numerical approaches," *Nuclear Engineering and Design*, no. 10, pp. 3372–3386, 2010.
- [12] L. Bělovský, J. Gadò, B. Hatala, A. Vasile and G. Wrochna, "The ALLEGRO Experimental Gas Cooled Fast Reactor Project," in *International Conference on Fast Reactor and Related Fuel Cycles, Next Generation Nuclear Systems for Sustainable Development*, Yekaterinburg, Russia, June 26–29, 2017.
- [13] E. E. Dominguez-Ontiveros and Y. A. Hassan, "Non-intrusive experimental investigation of flow behavior inside a 5x5 rod bundle with spacer grids using PIV and MIR," *Nuclear Engineering and Design*, no. 5, pp. 888–898, 2009.

Formattato: Interlinea: multipla 1.3 ri

Formattato: Interlinea: multipla 1.3 ri

Formattato: Interlinea: multipla 1.3 ri

Formattato: Interlinea: multipla 1.3 ri

Formattato: Interlinea: multipla 1.3 ri

Formattato: Interlinea: multipla 1.3 ri

Formattato: Interlinea: multipla 1.3 ri

Formattato: Interlinea: multipla 1.3 ri

Formattato: Interlinea: multipla 1.3 ri

Formattato: Interlinea: multipla 1.3 ri

Formattato: Interlinea: multipla 1.3 ri

Formattato: Interlinea: multipla 1.3 ri

Formattato: Interlinea: multipla 1.3 ri

Formattato: Interlinea: multipla 1.3 ri

Formattato: Interlinea: multipla 1.3 ri

Formattato: Interlinea: multipla 1.3 ri

Formattato: Interlinea: multipla 1.3 ri

Formattato: Interlinea: multipla 1.3 ri

Formattato: Interlinea: multipla 1.3 ri

[14] S. Jun, "The Progress of HTR-PM in China," in *Small and Advanced Reactors [Online Conference]*, Institute of Nuclear and New Energy Technology, Tsinghua University, Beijing, China, February 18, 2021.

[15] W. J. Kim, D. Kim and J. Y. Park, "Fabrication and Material Issues for the Application of SiC Composites to LWR Fuel Cladding," *Nuclear Engineering and Technology*, no. 4, pp. 565-572, 2013.

[16] Y. Lee, T. J. McKrell and M. S. Kazimi, "Thermal-shock fracture of hot silicon carbide immersed in water," *Journal of Nuclear Materials*, p. 172-180, 2015.

[17] A. Papukchiev and S. Buchholz, "Validation of ANSYS CFX for gas and liquid metal flows with conjugate heat transfer within the European project THINS," *Nuclear Engineering and Design*, p. 338-350, 2017.

[18] P. Qi, P. Wang, S. Hao, K. Cheng, S. Qiao and S. Tan, "Experimental study of flow structures in a large range downstream the spacer grid in a 5 × 5 rod bundle using TR-PIV," *International Journal of Heat and Fluid Flow*, 108619, 2020.

[19] W. Qu, J. Xiong, S. Chen and X. Cheng, "High-fidelity PIV measurement of cross flow in 5x5 rod bundle with mixing vane grids," *Nuclear Engineering and Design*, pp. 131-143, 2019.

[20] Z. Zhang, Y. Dong, F. Li, Z. Zhang, H. Wang, X. Huang, H. Li, B. Liu, X. Wu, H. Wang, X. Diao, H. Zhang and J. Wang, "The Shandong Shidao Bay 200 MWe High Temperature Gas-Cooled Reactor Pebble-Bed Module (HTR-PM) Demonstration Power Plant: An Engineering and Technological Innovation," *Engineering*, no. 1, pp. 112-118, 2016.

Formattato: Interlinea: multipla 1.3 ri

Formattato: Interlinea: multipla 1.3 ri

Formattato: Interlinea: multipla 1.3 ri

Formattato: Interlinea: multipla 1.3 ri

Formattato: Interlinea: multipla 1.3 ri

Formattato: Interlinea: multipla 1.3 ri

Formattato: Interlinea: multipla 1.3 ri

Formattato: Interlinea: multipla 1.3 ri

Formattato: Interlinea: multipla 1.3 ri

Formattato: Interlinea: multipla 1.3 ri

Formattato: Interlinea: multipla 1.3 ri

Formattato: Interlinea: multipla 1.3 ri

Formattato: Interlinea: multipla 1.3 ri

Formattato: Interlinea: multipla 1.3 ri

ha formattato: Italiano (Italia)

Formattato: Allineato a sinistra, Interlinea: multipla 1.3 ri